

Wasserstein Gradient Flows for Scalable and Regularized Barycenter Computation

Eduardo Fernandes Montesuma¹Yassir Bendou¹Mike Gartrell¹¹Sigma Nova, Paris, France

Abstract

Wasserstein barycenters provide a principled approach for aggregating probability measures, while preserving the geometry of their ambient space. Existing discrete methods are not scalable as they assume access to the complete set of samples from the input measures. Meanwhile, neural network approaches do scale well, but rely on complex optimization problems and cannot easily incorporate label information. We address these limitations through gradient flows in the space of probability measures. Through time discretization, we achieve a scalable algorithm that i) relies on mini-batch optimal transport, ii) accepts modular regularization through task-aware functions, and iii) seamlessly integrates supervised information into the ground-cost. We empirically validate our approach on domain adaptation benchmarks that span computer vision, neuroscience, and chemical engineering. Our method establishes a new state-of-the-art barycenter solver, with labeled barycenters consistently outperforming unlabeled ones.

1 INTRODUCTION

Defining the mean or center of a set of probability measures is a fundamental primitive in geometric probability theory [Nielsen, 2020]. Given $K \in \mathbb{N}$ probability measures $\mathcal{Q} = \{Q_k\}_{k=1}^K$ on a metric space (Ω, d) , their *Wasserstein barycenter* [Aagueh and Carlier, 2011] is given by,

$$P^* = \arg \min_{P \in \mathcal{P}_2(\Omega)} \left\{ \mathbb{B}(P) = \sum_{k=1}^K \lambda_k \mathbb{W}_2(P, Q_k)^2 \right\}, \quad (1)$$

where $\mathcal{P}_2(\Omega)$ is the set of measures over Ω with finite second moments, and $\lambda = (\lambda_1, \dots, \lambda_k)$, $\lambda_k \geq 0, \forall k, \sum_k \lambda_k = 1$ is an array of *barycentric coordinates*. Equation 1 defines a

notion of average of the input measures in \mathcal{Q} . The main advantage of these barycenters stems from Optimal Transport (OT) [Villani, 2008], that is, they *lift* the geometry of the space (Ω, d) to the space $(\mathcal{P}_2(\Omega), \mathbb{W}_2)$ [Kloeckner, 2010].

Wasserstein barycenters have wide applications to machine learning, such as posterior aggregation in Bayesian inference [Srivastava et al., 2018], model fusion [Singh and Jaggi, 2020], ensembling in time series forecasting [Coz et al., 2023], data augmentation [Zhu et al., 2023], and Domain Adaptation (DA) [Montesuma and Mboula, 2021, Montesuma et al., 2023, 2024b]. In each application, the main advantage is geometric fidelity, that is, the Wasserstein barycenter captures and preserves the underlying structure of samples. Figure 1 shows a conceptual illustration.

Despite its advantages, Wasserstein barycenters remain challenging beyond the Gaussian setting [Altschuler and Boix-Adsera, 2022]. We have identified three gaps in the current literature. First, the seminal algorithm of Cuturi and Doucet [2014] requires having access to the complete set of input measures' samples at once, making it intractable for large datasets. Neural network methods [Fan et al., 2020, Korotin et al., 2021, Kolesov et al., 2024, Gazdieva et al., 2024] alleviate this issue by operating on mini-batches, but parametrize the barycentric measure with $\mathcal{O}(K)$ neural networks, coupling model complexity with the number of input measures. Second, neural methods cannot seamlessly incorporate label information into their ground-cost, limiting their performance in supervised tasks (cf. Table 2). Third, the objective function in equation 1 only accounts for distributional fit. In practice, the barycentric measure must satisfy additional structural properties, such as class separation. Current **barycenter solvers** do not offer a principled way of enforcing these properties.

Recent methods study the barycenter problem through the gradient flow perspective. First, Chewi et al. [2020] established a gradient flow algorithm on the Bures-Wasserstein manifold, i.e., on Gaussian measures. Second, Chizat [2025] describes the *doubly regularized* barycenter prob-

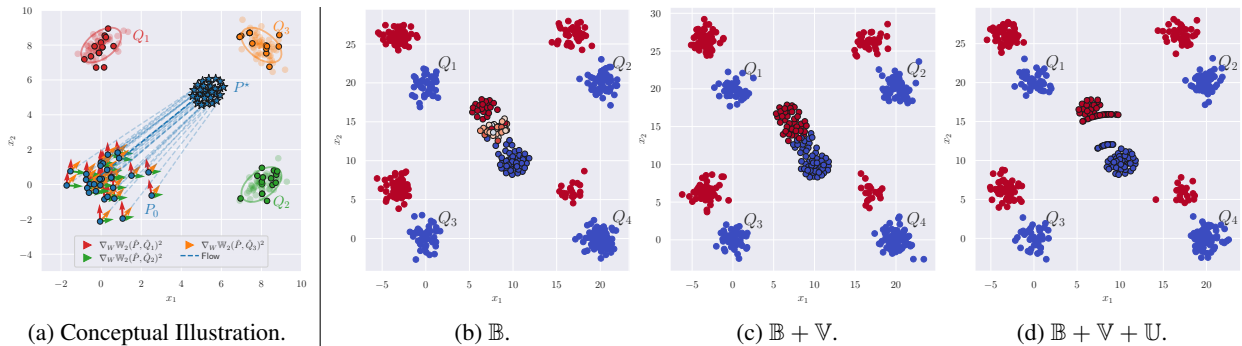


Figure 1: In (a), we show an illustration of our flow. We show the initial barycenter measure P_0 which flow towards the solution P^* . In red, green, and orange, we show the input measures’ mini-batches as solid dots. The flow is given by the combination of gradients $v_{\tau,i} = \sum_{k=1}^K \lambda_k \nabla \mathbb{W}_2(P_{\tau}, Q_k)$. In parallel, (b) shows a pathological barycenter calculation, with fuzzy labels and unclear class boundaries. Adding regularizers \mathbb{V} (b) and \mathbb{U} (c) progressively resolves this issue.

lem through the same lens. Here, in addition to *entropic regularization* at the level of OT, they proposed an *outer regularization* that penalizes the entropy of the barycentric measure, which leads to a Noisy Particle Gradient Descent (NPGD) algorithm for empirical measures. Although this algorithm incorporates outer regularization, it has the same limitation as Cuturi and Doucet [2014], as it assumes *full-batch* access to the samples of input measures.

We address the aforementioned challenges through the lens of *gradient flows* in the space of probability measures [Ambrosio et al., 2008, Santambrogio, 2017]. We therefore conceptualize the barycenter problem as the flow from an initial measure $P_0 = \mathcal{N}(0, \text{Id})$ following the Wasserstein gradient of the functional,

$$\mathbb{F}(P) = \mathbb{B}(P) + \mathbb{R}(P), \quad (2)$$

where \mathbb{B} denotes the barycenter functional (cf. equation 1), and \mathbb{R} denotes additional regularizing functionals (see Sections 2.3 and 3.3, and Appendix C.2).

Following the established gradient flow literature [Santambrogio, 2017], we decompose \mathbb{R} into internal, potential, and interaction energies, denoted \mathbb{G} , \mathbb{V} , and \mathbb{U} , respectively. This decomposition generalizes the double regularization strategy of Chizat [2025]. Indeed, setting $\mathbb{V} = \mathbb{U} = 0$ and $\mathbb{G}(P) = \eta_G H(P)$, where $H(P)$ denotes the entropy of P , corresponds to their exact framework. Similarly, Alvarez-Melis and Fusi [2021] devised an approach for flowing a single dataset towards a known target. Our setting differs structurally from that. First, we go beyond the single measure objective, optimizing the *multi-measure* barycentric objective (cf. equation 1). Second, while Alvarez-Melis and Fusi [2021] *transforms* an existing dataset towards a known target, ours *synthesizes* a measure (i.e., the barycentric measure) from noise.

Our contributions are as follows. (i) **A mini-batch, time discretized gradient flow algorithm for regularized empirical Wasserstein barycenters (Algorithm 1)**. By randomly

sampling the input measures, we reduce the computational complexity of traditional barycenter methods [Cuturi and Doucet, 2014, Montesuma et al., 2023, Chizat, 2025] achieving $2\times$ to $50\times$ speedups with respect to discrete solvers (Figure 5). (ii) **Modular, task-aware regularizing functionals for Wasserstein barycenters (Section 3.3)**. Following previous gradient flow literature [Santambrogio, 2017, Alvarez-Melis and Fusi, 2021], we decompose \mathbb{R} into internal, potential, and interaction energies, allowing incorporation of plug-and-play regularizers into the barycenter problem. This goes beyond Chizat [2025], who considered a particular internal energy as an outer regularization strategy. (iii) **Extensive DA benchmarking (Section 4)**. We empirically show that our algorithm produces barycenters that respect class structure, by incorporating both appropriate functionals (Section 3.3), and labels into the ground-cost of optimal transport (Section 3.2). On 5 DA benchmarks, spanning computer vision, neuroscience, and chemical engineering, we establish a comparison between empirical and neural barycenter solvers, showing that structured costs are essential for DA performance.

Paper organization. Section 2 reviews OT, Wasserstein barycenters and gradient flows. Section 3 develops our empirical, time-discretized gradient flow framework and algorithms. Section 4 presents our experiments. Finally, Section 5 concludes this paper.

2 BACKGROUND

Throughout this paper (Ω, d) is a metric space, and its elements are denoted $z \in \Omega$. We denote $\mathcal{P}_2(\Omega)$ as the set of measures with finite second moments [Villani, 2008, Definition 6.4]. We work with empirical measures,

$$\text{Emp}_n(\Omega) = \left\{ \hat{P} \in \mathcal{P}_2(\Omega) : \hat{P} = \frac{1}{n} \sum_{i=1}^n \delta_{z_i^{(P)}} \right\}, \quad (3)$$

where $\delta_{z_0}(z) = \delta(z - z_0)$ denotes the Dirac measure centered at $z_0 \in \Omega$. Given a measure $P \in \mathcal{P}_2(\Omega)$, we denote by $\hat{P} \in \text{Emp}_n(\Omega)$ its empirical approximation based on i.i.d. samples $z_1^{(P)}, \dots, z_n^{(P)} \sim P$. The superscript $\cdot^{(P)}$ indicates the measure from which the samples originate.

2.1 OPTIMAL TRANSPORT

OT is a field of mathematics [Villani, 2008] concerned with mass transportation at least effort [Peyré and Cuturi, 2019, Montesuma et al., 2025]. It was originally founded by Monge [1781], and seeks a mapping such that,

$$T_{P \rightarrow Q}^* = \arg \inf_{T_{\#} P = Q} \mathbb{E}_{z \sim P} [d(z, T(z))^2]. \quad (4)$$

$T_{P \rightarrow Q}^*$ is an OT mapping between P and Q , and $T_{\#}$ is the pushforward mapping P to Q . Alternatively, Kantorovich [1942] proposed a formulation in terms of a transport plan $\gamma \in \Gamma(P, Q)$, where $\Gamma(P, Q)$ is the set of all joint measures with marginals P and Q . In this case,

$$\gamma^* = \arg \inf_{\gamma \in \Gamma(P, Q)} \mathbb{E}_{(z, z') \sim \gamma} [d(z, z')^2], \quad (5)$$

where γ^* denotes an OT plan. OT defines the so-called 2–Wasserstein distance, through the infimum value of the optimization problem in equations 4 and 5,

$$\mathbb{W}_2(P, Q)^2 = \inf_{\gamma \in \Gamma(P, Q)} \mathbb{E}_{(z, z') \sim \gamma} [d(z, z')^2]. \quad (6)$$

Equation 6 defines a metric in $\mathcal{P}_2(\Omega)$ which bridges the notions of Euclidean (i.e., center of mass) and Wasserstein barycenters. An alternative consists of regularizing the OT problem with the entropy of γ , resulting in the Sinkhorn divergence Cuturi [2013],

$$\mathbb{W}_{2,\epsilon}(P, Q)^2 = \inf_{\gamma \in \Gamma(P, Q)} \mathbb{E}[d(z, z')^2] + \lambda H(\gamma), \quad (7)$$

where $H(\gamma) = \text{KL}(\gamma | P \otimes Q)$, for $(P \otimes Q)(z) = P(z)Q(z)$, and KL is the Kullback Leibler divergence. Equation 7 enjoys many desirable properties. First, by relying on the matrix scaling algorithm of Sinkhorn [1964], it has complexity $\mathcal{O}(n^2)$ per iteration. Second, it can be vectorized in modern GPUs, leading to dramatic speed ups. Third, since $H(\gamma)$ is strictly convex, the overall optimization problem in equation 7 is convex, leading to a unique solution.

2.2 WASSERSTEIN BARYCENTER

In the metric setting, the barycenter problem is known as Fréchet [1948] or Karcher [1977] means. In our case, given a finite family of measures $\mathcal{Q} = \{Q_k\}_{k=1}^K$ and a set of barycentric coordinates $\lambda \in \Delta_K = \{a \in \mathbb{R}_{\geq 0}^K : \sum_k a_k = 1\}$, we define the Wasserstein barycenter over

$(\mathcal{P}_2(\Omega), \mathbb{W}_2)$ through the following optimization problem,

$$\hat{P}^* = \arg \min_{\hat{P} \in \text{Emp}_n(\Omega)} \left\{ \mathbb{B}_{2,\epsilon}(\hat{P} | \mathcal{Q}) = \sum_{k=1}^K \lambda_k \mathbb{W}_{2,\epsilon}(\hat{P}, \hat{Q}_k)^2 \right\}. \quad (8)$$

Here, $\mathbb{B}_{2,\epsilon}(\cdot | \mathcal{Q})$ is a functional mapping $\text{Emp}_n(\Omega)$ to $\mathbb{R}_{\geq 0}$, i.e., the set of non-negative real numbers. Henceforth, we denote $\mathbb{B}_\epsilon(\hat{P})$ for simplicity. We provide a further description of barycenter solvers in Appendix B.

2.3 GRADIENT FLOWS

Our method relies on the gradient flow interpretation of the minimization in equation 8. Starting from the Euclidean setting, let $F : \mathbb{R}^d \rightarrow \mathbb{R}$ be a functional. A gradient flow is the solution to the Ordinary Differential Equation (ODE),

$$\dot{x}(t) = -\nabla F(x(t)), \text{ subject to } x(0) = x_0. \quad (9)$$

This framework extends to probability measures. Let $\mathbb{F} : \mathcal{P}_2(\Omega) \rightarrow \mathbb{R}$ be a functional over $\mathcal{P}_2(\Omega)$. The evolution of a curve $\{P_t\}_{t \geq 0}$ in $\mathcal{P}_2(\Omega)$ is given by the continuity equation

$$\partial_t P_t = -\text{div}(P_t v_t), \quad (10)$$

where $v_t : \Omega \rightarrow \Omega$ is a velocity field, and div is the divergence operator, understood in a measure theoretic sense. Choosing $v_t = -\nabla_W \mathbb{F}(P_t)$ yields the gradient flow of \mathbb{F} , that is, the measure theoretic analogue of equation 9. Here, ∇_W denotes the Wasserstein gradient of the functional \mathbb{F} (c.f. [Chewi et al., 2024, Section 5.4] and appendix C.1).

The structure of \mathbb{F} determines the dynamics of P_t . Following the classical OT theory [Santambrogio, 2015, Chapter 7], we consider the functional $\mathbb{F}(P) = \mathbb{B}(P) + \mathbb{R}(P)$, where,

$$\begin{aligned} \mathbb{R}(P) = & \underbrace{\int G(p(z)) dz}_{\text{Internal energy } \mathbb{G}(P)} + \underbrace{\int V(z) dP(z)}_{\text{Potential energy } \mathbb{V}(P)} + \\ & \underbrace{\int \int U(z, z') dP(z) dP(z')}_{\text{Interaction energy } \mathbb{U}(P)} \end{aligned} \quad (11)$$

where $p : \Omega \rightarrow \mathbb{R}$ denotes the density of P , $G : \mathbb{R} \rightarrow \mathbb{R}$, $V : \Omega \rightarrow \mathbb{R}$, and $U : \Omega \times \Omega \rightarrow \mathbb{R}$. For example, when $G(s) = s \log s$, \mathbb{G} is the *entropy functional* of [Chizat, 2025], associated with diffusion dynamics. \mathbb{G} , \mathbb{V} , and \mathbb{U} introduce diffusion, drift, and pairwise behaviors in the flow, respectively. See Section 3.3 for further examples.

3 WASSERSTEIN BARYCENTERS AS GRADIENT FLOWS

In this section, we describe a new method for computing empirical OT barycenters. We use,

$$\mathbb{F}(\hat{P}) = \mathbb{B}_\epsilon(\hat{P}) + \mathbb{R}(\hat{P}), \quad (12)$$

where $\mathbb{B}_\epsilon(\hat{P})$ is the barycenter objective defined in Equation 8, and \mathbb{R} is a combination of different energies defined in Equation 11. We implement a flow from a prior measure $P_0 = \mathcal{N}(0, \text{Id})$ to $\hat{P}^* = \min_{\hat{P} \in \text{Emp}_n(\Omega)} \mathbb{F}(\hat{P})$ through a time-discretized version of the continuity equation. We proceed in two steps.

First, we derive the empirical version of the continuity equation (c.f., Equation 10). For $\hat{P}_t \in \text{Emp}_n(\Omega)$:

$$\begin{aligned} \partial_t \hat{P}_t &= \frac{1}{n} \sum_{i=1}^n \partial_t \delta_{z_{t,i}^{(P)}} = -\frac{1}{n} \sum_{i=1}^n \text{div}(\dot{z}_{t,i}^{(P)} \delta_{z_{t,i}^{(P)}}), \quad (13) \\ &= -\text{div}(\hat{P}_t v_t), \end{aligned}$$

where we identified $v_t(z_{t,i}^{(P)}) = \dot{z}_{t,i}^{(P)}$. Second, we discretize the gradient flow in time, through an index $\tau = \alpha t$, $\alpha > 0$. Using the forward Euler scheme,

$$\dot{z}_{t,i}^{(P)} = \frac{z_{\tau+1,i}^{(P)} - z_{\tau,i}^{(P)}}{\alpha} \rightarrow z_{\tau+1,i}^{(P)} = z_{\tau,i}^{(P)} + \alpha v_{\tau,i}, \quad (14)$$

where $v_{\tau,i} = v_\tau(z_{\tau,i}^{(P)})$. We can obtain different update strategies based on the velocity field,

$$v_{\tau,i} = -\nabla_{z_{\tau,i}^{(P)}} \mathbb{F}(\hat{P}_\tau), \quad (15)$$

$$v_{\tau,i} = -\nabla_{z_{\tau,i}^{(P)}} \mathbb{F}(\hat{P}_\tau) + \sqrt{2\alpha\eta_G} \eta_{\tau,i}, \quad (16)$$

$$v_{\tau,i} = u_{\tau,i}, \quad u_{\tau+1,i} = \beta u_{\tau,i} - \alpha \nabla_{z_{\tau,i}^{(P)}} \mathbb{F}(\hat{P}_\tau). \quad (17)$$

Equations 15, 16 and 17 correspond to the steepest descent, Langevin dynamics, and momentum descent strategies, respectively. $\eta_G \geq 0$ denotes the diffusion coefficient. The Langevin dynamics version of the flow corresponds to the NPGD dynamics of Chizat [2025]. Furthermore, for empirical measures, the functionals in Equation 12 are tractable, and take the following form,

$$\begin{aligned} \mathbb{B}_\epsilon(\hat{P}) &= \sum_{k=1}^K \lambda_k \sum_{i=1}^n \sum_{j=1}^{n_k} \gamma_{\epsilon,k,i,j}^* d(z_i^{(P)}, z_j^{(Q_k)})^2, \\ \mathbb{G}(\hat{P}) &= \frac{1}{n} \sum_{i=1}^n G(\hat{p}(z_i^{(P)})), \\ \mathbb{V}(\hat{P}) &= \frac{1}{n} \sum_{i=1}^n V(z_i^{(P)}), \\ \mathbb{U}(\hat{P}) &= \frac{1}{n^2} \sum_{i=1}^n \sum_{j=1}^n U(z_i^{(P)}, z_j^{(P)}), \end{aligned} \quad (18)$$

where \hat{p} denotes the density of \hat{P} . Since \hat{P} is empirical it is, in general, difficult to compute \mathbb{G} . A notable exception is the entropy functional (i.e., $G(s) = s \log s$), which adds a diffusion term to the gradient flow dynamics. This corresponds to Langevin dynamics [Chizat, 2025] (Equation 16). For general choices of G , one needs to estimate the density \hat{p} at each iteration of the empirical flow.

Algorithm 1 Empirical Time Discretized Wasserstein Gradient Flow

Input: $\lambda \in \Delta_K$, $n \in \mathbb{N}$, $m \in \mathbb{N}$, $\alpha \in \mathbb{R}_+$, $\epsilon \in [0, +\infty)$

Output: Barycenter support $\{z_i^{(P)}\}_{i=1}^n$

- 1: $\{z_{0,i}^{(P)}\}_{i=1}^n$, such that $z_{0,i}^{(P)} \sim \mathcal{N}(0, \text{Id})$.
- 2: **for** $\tau \leftarrow 1$ to n_{iter} **do**
- 3: $\mathbb{F}(\hat{P}_\tau) \leftarrow \mathbb{V}(\hat{P}_\tau) + \mathbb{U}(\hat{P}_\tau) + \mathbb{G}(\hat{P}_\tau)$
- 4: **for** $k \leftarrow 1$ to K **do**
- 5: Sample $\{z_i^{(Q_k)}\}_{i=1}^m$ i.i.d. from Q_k .
- 6: $\mathbb{F}(\hat{P}_\tau) \leftarrow \mathbb{F}(\hat{P}_\tau) + \lambda_k \mathbb{W}_{2,\epsilon}(\hat{P}_\tau, Q_k)^2$
- 7: **end for**
- 8: $z_{\tau+1,i}^{(P)} \leftarrow z_{\tau,i}^{(P)} + \alpha v_{\tau,i}$
- 9: **end for**

An immediate consequence of Equation 18 is that our gradient flow formulation encompasses several previous works. For instance, with $G = U = V = 0$, we have the classical free-support barycenters of Cuturi and Doucet [2014]. Furthermore, for the entropy functional and $\epsilon > 0$, we have the NPGD algorithm of Chizat [2025]. Finally, as we show in Section 3.2 below, with a specific metric on $\Omega = \mathcal{X} \times \mathcal{Y}$, we retrieve the algorithm of Montesuma et al. [2023].

3.1 SCALING WITH MINI-BATCH OT

The computation of \mathbb{B}_ϵ in the discrete approach [Cuturi and Doucet, 2014] involves an OT problem between the complete set of samples in the input measures. Therefore, when the input measures are large scale, the barycenter problem becomes infeasible. We circumvent this issue with mini-batch OT [Fratras et al., 2021].

The main idea behind our scalable barycenter algorithm is accessing $Q_k \in \mathcal{Q}$ through sampling. At each iteration of Algorithm 1, we sample a mini-batch $\{z_i^{(Q_k)}\}_{i=1}^m$ of m samples from each input measure (cf. line 5 in Algorithm 1). Since we sample the same number of samples from each measure, we can actually vectorize the computation of the K OT problems in the evaluation of $\mathbb{W}_{2,\epsilon}$.

Let $\{z_{\tau,i}^{(P)}\}_{i=1}^n$ be the barycenter support, and $\{z_j^{(Q_k)}\}_{j=1}^m$ be a mini-batch from Q_k . The Gibbs kernel $E_{k,i,j} = e^{-(C_{k,i,j}/\epsilon)}$, and $C_{k,i,j} = d(z_{\tau,i}^{(P)}, z_j^{(Q_k)})^2$ are arrays with shape (K, n, m) . The Sinkhorn iterations become,

$$\psi_k^{(\ell+1)} = \frac{b}{E_k^T \phi_k^{(\ell)}}, \text{ and } \phi_k^{(\ell+1)} = \frac{a_k}{E_k \psi_k^{(\ell+1)}}, \quad (19)$$

where the division operation should be understood coordinate-wise. Furthermore, $b_j = n^{-1}$ and $a_{k,i} = m^{-1}$ is the importance of each sample in the barycenter, and input measure support, respectively. For simplicity, we assume uniform weights. For $L \in \mathbb{N}$ iterations, we can retrieve $\gamma_{\epsilon,k}^* = \text{diag}(\phi_k^{(L)}) E_k \text{diag}(\psi_k^{(L)})$. Since each $\gamma_{\epsilon,k}^*$ has

shape (n, m) , we can actually stack it in an array of shape (K, n, m) , similarly to E and C .

The main advantage of equation 19 is that **the K OT problems can be vectorized**. This is possible because we draw the same number of samples from each input measure, making it possible to vectorize the Sinkhorn iterations. For instance, a similar strategy is possible for measures over a fixed grid [Peyré and Cuturi, 2019, Remark 4.16]. The OT plan γ_ϵ , obtained at the end of the Sinkhorn iterations, is used to compute \mathbb{B}_ϵ , in lines 4 through 7 in Algorithm 1.

3.2 FLOWS OVER JOINT MEASURES

An interesting advantage of the gradient flow formalism is that the only necessary ingredient is a differentiable metric over Ω . Therefore, we generalize the setting of Cuturi and Doucet [2014], who assumed $\Omega = \mathbb{R}^d$, and $d(z, z') = \|z - z'\|_2$. As we show in our experiments, in machine learning applications one has $\Omega = \mathcal{X} \times \mathcal{Y}$, i.e., measures over the joint space of features and labels. Let $z = (x, y)$, $x \in \mathcal{X}$, $y \in \mathcal{Y}$,

$$d(z, z') = \sqrt{\|x - x'\|_2^2 + \beta \|y - y'\|_2^2}, \quad (20)$$

where $\beta \geq 0$ is a parameter that balances the feature distance terms and the label distance terms.

For regression applications (i.e., $\mathcal{Y} = \mathbb{R}$), this distance is quite natural. However, for classification, \mathcal{Y} is categorical (e.g., $\mathcal{Y} = \{1, \dots, n_{\text{classes}}\}$). One possible strategy, used in Montesuma and Mboula [2021] and Alvarez-Melis and Fusi [2021], is fixing the labels and flowing only the features. In contrast to these works, we embed \mathcal{Y} into the compact continuous space $\Delta_{n_{\text{classes}}}$, through a one-hot encoding operation. For our flow, we parametrize labels through a change of variables,

$$y_{i,c}^{(P)} = \text{softmax}(\ell_{i,1}^{(P)}, \dots, \ell_{i,n_c}^{(P)}) = \frac{\exp(\ell_{i,c}^{(P)})}{\sum_{c=1}^{n_c} \exp(\ell_{i,c}^{(P)})},$$

thus, instead of optimizing over $z = (x, y)$, we optimize over $z = (x, \ell)$, $x \in \mathbb{R}^d$, $\ell \in \mathbb{R}^{n_{\text{classes}}}$. From the soft probabilities, we can retrieve the actual discrete labels with an argmax , $y_{\text{hard},i}^{(P)} = \text{argmax}_{c=1, \dots, n_c} y_{i,c}^{(P)}$.

3.3 TASK-AWARE REGULARIZING FUNCTIONALS

One of the advantages of our proposed method is regularizing the barycenter calculation with internal, interaction, and potential energy functionals. This idea was already used in practice by Alvarez-Melis and Fusi [2021] for transfer learn-

ing problems. Here we propose the following functionals,

$$V_E(z) = -\eta_V \sum_{c=1}^{n_{\text{classes}}} y_c \log y_c, \quad (21)$$

$$U_R(z, z') = \begin{cases} \eta_U h(d(x, x')) & \text{if } y_{\text{hard}} \neq y'_{\text{hard}}, \\ 0 & \text{otherwise} \end{cases}, \quad (22)$$

where $h : \mathbb{R} \rightarrow \mathbb{R}$ is lower semi-continuous and bounded from below, and $\eta_V > 0$ and $\eta_U > 0$ are scaling parameters. For instance, in our experiments we use the hinge loss, $h(u) = \max(0, \text{margin} - d)$, where $\text{margin} \geq 0$ is a margin parameter. Equations 21 and 22 correspond to entropy and repulsion, respectively. The first functional penalizes barycenters that have fuzzy labels. The second functional encourages classes to be well separated.

3.4 CONVERGENCE

One of the difficulties in analyzing the gradient flow of the functional in equation 12 comes from the fact that $P \mapsto \mathbb{W}_2(P, Q)^2$ is not geodesically convex in $\mathcal{P}_2(\Omega)$ [Santambrogio, 2017, Section 4.4]. As a result, we are minimizing a non-convex functional. **Explicit constants and proofs are available in Appendix D**. Our analysis relies on a measure-theoretic version of the Polyak Łojasiewicz (PL) inequality [Polyak, 1964, Karimi et al., 2016],

$$\|\nabla_W \mathbb{B}(P)\|_{L_2(P)}^2 \geq C_{\text{PL}} (\mathbb{B}(P) - \mathbb{B}^*). \quad (23)$$

When this inequality holds, we have the following convergence result.

Theorem 3.1. *Let $\Omega = \mathcal{B}(0, R)$ be the closed ball in \mathbb{R}^d with radius $R > 0$. Let $P^* \in \mathcal{P}_2(\Omega)$ be the barycenter of $\mathcal{Q} = \{Q_k\}_{k=1}^K$, $Q_k \in \mathcal{P}_2(\Omega)$ $k = 1, \dots, K$, with barycentric coordinates $\lambda = (\lambda_1, \dots, \lambda_K) \in \Delta_K$. Approximate each Q_k with m i.i.d. samples $\{z_i^{(Q_k)}\}_{i=1}^m$, $z_i^{(Q_k)} \sim Q_k$ and $\{z_{\tau,i}^{(P)}\}_{i=1}^n$ be the barycenter support. Under inequality 42 the following holds,*

$$\mathbb{E}[\hat{\mathbb{B}}(\hat{P}_\tau) - \hat{\mathbb{B}}^*] \leq e^{-C_{\text{PL}}\tau} (\mathbb{B}(\hat{P}_0) - \mathbb{B}^*) + C_R \sqrt{\frac{C_{d,n}}{m}}, \quad (24)$$

where the expectation is taken with respect to samples from Q_k . The constants C_R and $C_{d,n}$ depend on the radius R , number of barycenter samples n , and dimensions d . m denotes the number of samples drawn from each Q_k .

The first term in the r.h.s. of equation 24 decays exponentially with the iterations τ , and is a direct consequence of the PL inequality in equation 23. The second term captures the empirical approximation error of the involved measures, that is, $Q_k \in \mathcal{Q}$ and P_τ . In practice, $\tau \rightarrow +\infty$ leads to an error governed by the empirical approximations.

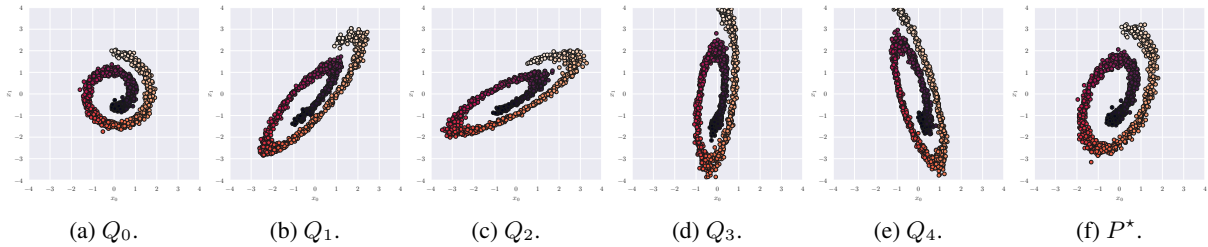


Figure 2: Swiss roll measures in a location-scatter family, where a source measure is transformed under an affine function $T_k(x) = A_k x + b_k$. Colors reflect the relative position of points in the manifold.

On the PL Inequality. Equation 23 is a standard tool used in proving the convergence of non-convex optimization algorithms, however, it is an open question whether it holds in general settings. For instance, Chewi et al. [2020] shows that this inequality holds for Gaussian measures under specific spectral conditions. In the Appendix, we show that the same result holds for *location-scatter families of measures* (Appendix D.2), based on the isometry between these sets, and the Bures-Wasserstein manifold established by [Álvarez-Esteban et al., 2016, Theorem 2.3]. On top of this theoretical justification, we provide an experiment validating the bound on the Swiss roll measure (Appendix D.1).

4 EXPERIMENTS

In the following, all experiments were conducted on a virtual machine with 8 CPUs (AMD EPYC 7413, 48GB of RAM) and an NVIDIA L4 GPU (24GB of VRAM). Appendix F includes additional details, fine-grained results, complexity analysis and ablations.

4.1 SWISS ROLL MEASURES

In Figure 2, we show the Swiss roll measure [Korotin et al., 2021] Q_0 , alongside four variations obtained via $T_{k,\#}Q_0$, $k = 1, \dots, 4$, $T_k(x) = A_k x + b_k$, for which the ground-truth barycenter is known in closed-form [Álvarez-Esteban et al., 2016], that is, $P^* = (\sum_k \lambda_k T_k)_{\#}Q_0$. These measures are shown in Figure 2.

We compare 5 barycenter solvers, including discrete solvers [Cuturi and Doucet, 2014, Montesuma et al., 2023], and neural solvers: CW2B [Korotin et al., 2021], U-NOT Gazdieva et al. [2024], and NormFlow Visentin and Cheridito [2025]. First, we benchmark unsupervised solvers in Figures 3 (a) through (f). Quantitatively, empirical methods, notably [Cuturi and Doucet, 2014, Algorithm 2] and our Wasserstein Gradient Flow (WGF) algorithm (cf. Algorithm 1) achieve the lowest Wasserstein distance to the ground truth in Figure 2. Overall, while the neural network solvers are usually more scalable than discrete methods in terms of number of samples, their optimization is more complicated and very sensitive to hyper-parameters.

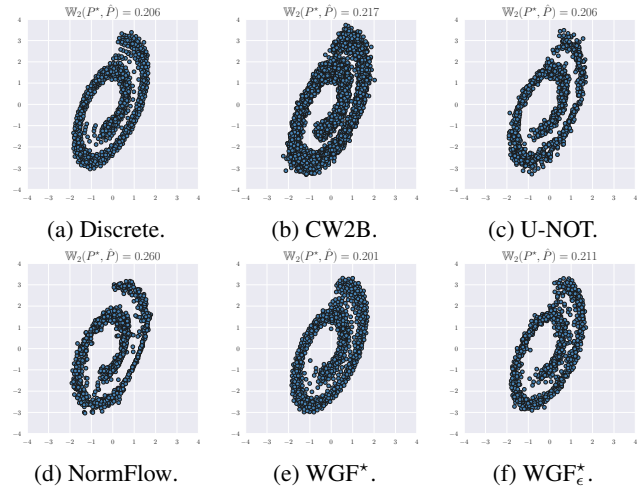


Figure 3: Comparison of unsupervised barycenter methods. Solvers (b, c, d) are neural, and (e, f) are ours.

Second, we experiment with integrating labels in the ground cost as described in Section 3.2. These methods are shown in Figures 4 (a), (b) and (c). In all cases, integrating labels produces barycenters that are closer to the ground-truth. We conclude that using the labels gives a strong inductive bias in the barycenter computation, which explains the gain in performance of labeled barycenters in the next section.

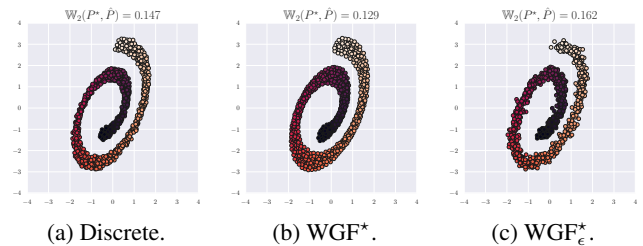


Figure 4: Comparison of supervised barycenter methods.

Next, we compare the running time of our WGF solver with the discrete solver of Cuturi and Doucet [2014], for an increasing barycenter support size $n \in \{2^{10}, \dots, 2^{16}\}$ and batch size $m \in \{2^8, 2^9, 2^{10}\}$ for 200 iterations. The discrete solver is run for $n \in \{2^{10}, \dots, 2^{14}\}$. For this algorithm,

larger support sizes **results in memory overflow**. Our WGF is able to compute larger barycenters via mini-batching.

We summarize our results in Figure 5. First, in Figure 5 (a), our WGF leads to speedups ranging from $2\times$ ($n = 2^{12}, m = 2^{10}$) to $50\times$ ($n = 2^{14}, m = 2^8$). Similar gains were obtained using Exact OT on CPU (Appendix F.3). Second, in Figure 5 (b), we isolate the gain of using GPU acceleration and our vectorization strategy (Section 3.1), showing consistent gains ranging from $2.1\times$ to $8.3\times$. Overall, our WGF strategy provides compounding speedups from three sources: (i) minibatching, (ii) entropic regularization, and (iii) GPU parallelism.

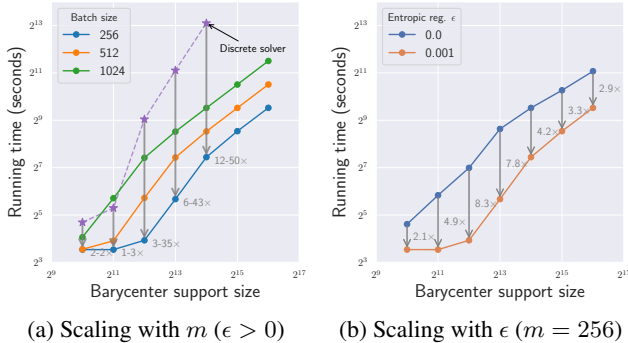


Figure 5: Running time analysis for our WGF algorithm. In (a), we compare the running time of our technique in comparison with the discrete solver of Cuturi and Doucet [2014]. In (b), we isolate the effect of GPU acceleration, showing consistent gains with increasing support size.

4.2 MULTI-SOURCE DOMAIN ADAPTATION

One of the main applications of Wasserstein barycenters is multi-source domain adaptation (MSDA) [Kouw and Loog, 2019, Sun et al., 2015, Pan and Yang, 2009]. In this setting one needs to adapt multiple labeled source measures Q_1, \dots, Q_K to a single unlabeled target measure Q_T . The goal is to learn, from samples $\{\{x_i^{(Q_k)}, y_i^{(Q_k)}\}_{i=1}^{n_k}\}_{k=1}^K$ and $\{x_i^{(Q_T)}\}_{i=1}^{n_T}$, a classifier h that achieves low risk or error in the target domain measure,

$$\mathcal{R}_{Q_T}(h) = \mathbb{E}_{(x,y) \sim Q_T}[\mathcal{L}(y, h(x))],$$

for a loss function \mathcal{L} (e.g., cross-entropy loss). We isolate the quality of barycenters by doing adaptation at the level of embeddings. This approach allows us to perform domain adaptation in a higher semantic space, where distributions are more meaningful and comparable across domains. Thus, we assume that a meaningful feature extractor ϕ , called the backbone, has been previously learned. We obtain the feature extractor by fine-tuning a neural network on the labeled source domain data (Appendix E.2).

Experimental Setup. The unsupervised WGF is fit with *unlabeled* measures, i.e., $Q_k = n_k^{-1} \sum_i \delta_{x_i^{(Q_k)}}$, where $x_i^{(Q_k)}$

are embedding vectors. The supervised WGF is fit with *labeled* measures, that is, $Q_k = n_k^{-1} \sum_{i=1}^{n_k} \delta_{(x_i^{(Q_k)}, y_i^{(Q_k)})}$. In both cases, $\hat{P} = n^{-1} \sum_{i=1}^n \delta_{(x_i^{(P)}, y_i^{(P)})}$ which allows us to apply the regularizing functionals defined in section 3.3.

Wasserstein Barycenter Transport. Montesuma and Mboula [2021] proposed a technique based on Wasserstein barycenters for domain adaptation. The idea is to map the synthesized barycenter support to the target domain through the barycentric mapping [Courty et al., 2016]. Then, a classifier can be learned on the target domain based on the transported data. We adapt this idea to unsupervised barycenter algorithms by using the computed barycenter as a pivot domain. See appendix E.4 for more details.

Benchmarks. We run our experiments on five benchmarks: Office 31 [Saenko et al., 2010], Office Home [Venkateswara et al., 2017], BCI-CIV-2a [Brunner et al., 2008], ISRUC [Khalighi et al., 2013], and TEP [Montesuma et al., 2024c]. The first two, second two, and last benchmarks correspond to computer vision, neuroscience, and chemical engineering benchmarks, respectively. We show in Table 1 an overview of our experimental setting.

Benchmark	Backbone	# Samples	# Domains	# Dim.	# Classes
Office31	ResNet50	3287	3	2048	31
BCI-CIV-2a	CBraMod	5184	10	200	4
TEP	CNN	17289	6	128	29
Office Home	ResNet101	15500	4	2048	65
ISRUC	CBraMod	89240	100	512	5

Table 1: Overview of benchmarks used for domain adaptation, sorted by number of samples.

Compared Methods. Overall, we compare seven Wasserstein barycenter strategies with ours. Besides those used in the previous section, we include the NOT approach of Kolesov et al. [2024], and the Gaussian Mixture Model (GMM) barycenter of Montesuma et al. [2024b]. For completeness, we include four other state-of-the-art methods in domain adaptation over embedding vectors. Those methods are: WJDOT Turrisi et al. [2022], DaDiL-R, and E Montesuma et al. [2023], and GMM-DaDiL Montesuma et al. [2024b]. For each benchmark, we use one domain as the target domain (e.g., Amazon vs. {dSLR, Webcam} in the Office 31 benchmark), and we measure the classification accuracy, i.e., the percentage of correct predictions.

Main Results. We present our main results in Table 2, which reports the average performance per domain on each benchmark. We provide fine-grained results in Appendix F. In general, labeled barycenter methods (the 3 last rows in Table 2) have a clear advantage over unsupervised methods. We argue that label information is essential in domain adaptation success, which is consistent with previous research [Courty et al., 2016, Montesuma and Mboula, 2021, Montesuma et al., 2023, 2024b]. Among barycenter methods, our WGF method achieves the best performance in all benchmarks,

outperforming previous methods in MSDA, such as WJDOT and DaDiL in the ISRUC, BCI-CIV, and TEP benchmarks.

Benchmark	$\mathcal{X} \times \mathcal{Y}$	Office31	OfficeHome	BCI-CIV-2a	ISRUC	TEP	Avg. Rank
Backbone	-	ResNet-50	ResNet-101	CBraMod	CBraMod	CNN	-
Source-Only	-	86.40	75.95	50.30	76.63	78.48	-
WJDOT	-	86.80	76.59	N/A	76.95	86.13	7.8
DaDiL-R	-	89.91	77.86	53.41	74.68	86.14	6.4
DaDiL-E	-	89.79	78.14	N/A	75.89	85.87	5.0
GMM-DaDiL	-	90.63	78.81	57.10	75.47	86.85	4.4
Discrete	\times	87.82	77.17	57.38	70.67	83.81	8.8
NormFlow	\times	86.80	76.73	55.45	78.04	82.89	10.0
CW2B	\times	86.37	76.44	57.25	75.84	85.83	9.0
NOT	\times	86.22	75.36	57.29	76.39	84.93	9.4
U-NOT	\times	86.97	76.85	57.17	77.06	85.43	7.8
WGF (ours)	\times	88.27	77.56	57.68	78.16	85.51	4.9
Discrete	\checkmark	87.93	77.09	57.43	78.20	86.09	5.0
GMM	\checkmark	88.54	77.87	57.04	74.58	84.67	8.2
WGF (ours)	\checkmark	89.52	78.42	57.68	80.02	86.87	1.9

Table 2: Average classification accuracy on target domains. The top group (WJDOT through GMM-DaDiL) include **general domain adaptation methods**. The middle and bottom groups show **barycenter solvers** without and with access to source labels ($\mathcal{X} \times \mathcal{Y} = \times$, $\mathcal{X} \times \mathcal{Y} = \checkmark$), respectively. Bold indicates best among barycenter methods.

Unsupervised vs. Supervised Barycenters. An intriguing finding of Table 2 is that, on some benchmarks, unsupervised WGF achieves decent performance, even outperforming supervised baselines (e.g., WJDOT of Turrisi et al. [2022]). We probe the reason why these methods have unreasonably good performance, by performing a t-SNE [Maaten and Hinton, 2008] visualization of the barycenter against the source domain samples, shown in Figure 6. We see that even without labels, the barycenter samples cluster around the classes. This effect stems from the geometry of the embeddings, which were optimized (through supervision on source domains) to separate classes. As a result, unsupervised OT already captures, to some extent, the cluster structure of the barycentric measure. Figures 6 (b) and (c) investigate the remaining performance gap, as we transport the measures towards the target. Figure 6 (b) shows the transported sources to the barycentric domain (left) and the synthesized barycenter (right), and Figure 6 shows the final transported samples in the target domain for the unsupervised strategy (left) and supervised one (right). We conclude that using a synthesized supervised barycenter is better than using an unsupervised barycenter as pivot domain (Appendix E.4). Therefore, *the inductive bias of using labels in the ground cost is essential for domain adaptation*. This further explains the performance of DaDiL methods, which directly synthesize the target domain through an approximate barycenter.

5 CONCLUSION

We have presented a new Wasserstein barycenter algorithm (Algorithm 1), inspired by the gradient flow literature Santambrogio [2015], that addresses two persistent challenges: scalability and regularization. We have derived a new algorithm that is amenable to mini-batch OT Fatras et al. [2021]

(Section 3.1). Under entropic OT, we further demonstrate that OT computations can be vectorized across the K input measures, leading to further speedups (Figure 5).

Our framework is flexible, and accommodates modular plugin regularization from internal, potential, and interaction energies (Section 3.3). Extensive experiments on domain adaptation demonstrate the value of our approach and that incorporating labels in the OT ground-cost is necessary for state-of-the-art performance (Table 2).

Finally, our work opens interesting research questions. First, our framework can be extended to more complex differentiable structures, such as Riemannian manifolds. Second, it opens the question on how to effectively integrate labels and other regularization schemes into neural network solvers.

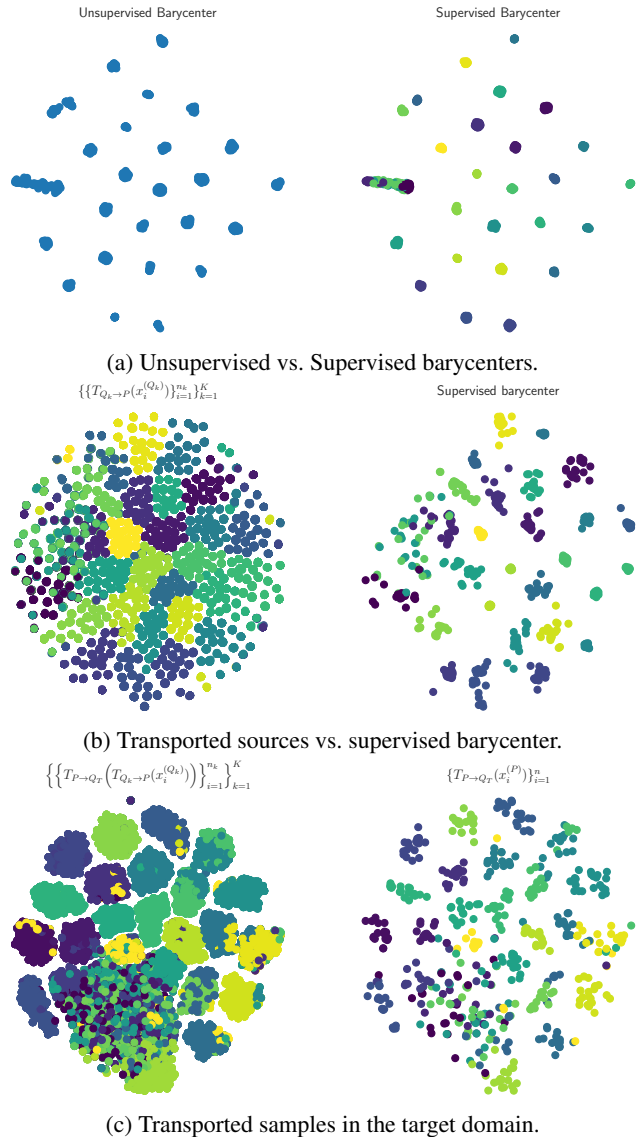


Figure 6: Comparison of unsupervised vs. supervised barycenter transports on the TEP benchmark.

References

- Martial Agueh and Guillaume Carlier. Barycenters in the wasserstein space. *SIAM Journal on Mathematical Analysis*, 43(2):904–924, 2011.
- Jason M Altschuler and Enric Boix-Adsera. Wasserstein barycenters are np-hard to compute. *SIAM Journal on Mathematics of Data Science*, 4(1):179–203, 2022.
- Pedro C Álvarez-Esteban, E Del Barrio, JA Cuesta-Albertos, and C Matrán. A fixed-point approach to barycenters in wasserstein space. *Journal of Mathematical Analysis and Applications*, 441(2):744–762, 2016.
- David Alvarez-Melis and Nicolò Fusi. Dataset dynamics via gradient flows in probability space. In *International conference on machine learning*, pages 219–230. PMLR, 2021.
- Luigi Ambrosio, Nicola Gigli, and Giuseppe Savaré. *Gradient flows: in metric spaces and in the space of probability measures*. Springer Science & Business Media, 2008.
- Julio Backhoff-Veraguas, Mathias Beiglböck, and Gudmun Pammer. Existence, duality, and cyclical monotonicity for weak transport costs. *Calculus of Variations and Partial Differential Equations*, 58(6):203, 2019.
- Nicolas Bonneel, Michiel Van De Panne, Sylvain Paris, and Wolfgang Heidrich. Displacement interpolation using lagrangian mass transport. In *Proceedings of the 2011 SIGGRAPH Asia conference*, pages 1–12, 2011.
- Yann Brenier. Polar factorization and monotone rearrangement of vector-valued functions. *Communications on pure and applied mathematics*, 44(4):375–417, 1991.
- Clemens Brunner, Robert Leeb, Gernot Müller-Putz, Alois Schlögl, and Gert Pfurtscheller. Bci competition 2008–graz data set a. *Institute for knowledge discovery (laboratory of brain-computer interfaces)*, Graz University of Technology, 16(1-6):34, 2008.
- Sinho Chewi, Tyler Maunu, Philippe Rigollet, and Austin J Stromme. Gradient descent algorithms for bures-wasserstein barycenters. In *Conference on Learning Theory*, pages 1276–1304. PMLR, 2020.
- Sinho Chewi, Jonathan Niles-Weed, and Philippe Rigollet. Statistical optimal transport. *arXiv preprint arXiv:2407.18163*, 3, 2024.
- Lénaïc Chizat. Doubly regularized entropic wasserstein barycenter. *Foundations of Computational Mathematics*, pages 1–38, 2025.
- Samuel Cohen, Michael Arbel, and Marc Peter Deisenroth. Estimating barycenters of measures in high dimensions. *arXiv preprint arXiv:2007.07105*, 2020.
- Nicolas Courty, Rémi Flamary, Devis Tuia, and Alain Rakotomamonjy. Optimal transport for domain adaptation. *IEEE transactions on pattern analysis and machine intelligence*, 39(9):1853–1865, 2016.
- Camille Le Coz, Alexis Tantet, Rémi Flamary, and Rival Plougonven. A barycenter-based approach for the multi-model ensembling of subseasonal forecasts. *arXiv preprint arXiv:2310.17933*, 2023.
- Marco Cuturi. Sinkhorn distances: Lightspeed computation of optimal transport. *Advances in neural information processing systems*, 26, 2013.
- Marco Cuturi and Arnaud Doucet. Fast computation of wasserstein barycenters. In *International conference on machine learning*, pages 685–693. PMLR, 2014.
- Nabarun Deb, Promit Ghosal, and Bodhisattva Sen. Rates of estimation of optimal transport maps using plug-in estimators via barycentric projections. *Advances in Neural Information Processing Systems*, 34:29736–29753, 2021.
- Jiaojiao Fan, Amirhossein Taghvaei, and Yongxin Chen. Scalable computations of wasserstein barycenter via input convex neural networks. *arXiv preprint arXiv:2007.04462*, 2020.
- Kilian Fatras, Younes Zine, Szymon Majewski, Rémi Flamary, Rémi Gribonval, and Nicolas Courty. Minibatch optimal transport distances; analysis and applications. *arXiv preprint arXiv:2101.01792*, 2021.
- Rémi Flamary, Nicolas Courty, Alexandre Gramfort, Mokhtar Z Alaya, Aurélie Boisbunon, Stanislas Chambon, Laetitia Chapel, Adrien Corenflos, Kilian Fatras, Nemo Fournier, et al. Pot: Python optimal transport. *Journal of Machine Learning Research*, 22(78):1–8, 2021.
- Maurice Fréchet. Les éléments aléatoires de nature quelconque dans un espace distancié. In *Annales de l’institut Henri Poincaré*, volume 10, pages 215–310, 1948.
- Wilfrid Gangbo and Robert J McCann. The geometry of optimal transportation. 1996.
- Milena Gazdieva, Jaemoo Choi, Alexander Kolesov, Jaewoong Choi, Petr Mokrov, and Alexander Korotin. Robust barycenter estimation using semi-unbalanced neural optimal transport. *arXiv preprint arXiv:2410.03974*, 2024.
- Ian J Goodfellow, Jean Pouget-Abadie, Mehdi Mirza, Bing Xu, David Warde-Farley, Shetjil Ozair, Aaron Courville, and Yoshua Bengio. Generative adversarial nets. *Advances in neural information processing systems*, 27, 2014.

- Nathael Gozlan, Cyril Roberto, Paul-Marie Samson, and Prasad Tetali. Kantorovich duality for general transport costs and applications. *Journal of Functional Analysis*, 273(11):3327–3405, 2017.
- Kaiming He, Xiangyu Zhang, Shaoqing Ren, and Jian Sun. Deep residual learning for image recognition. In *Proceedings of the IEEE conference on computer vision and pattern recognition*, pages 770–778, 2016.
- L Kantorovich. On the transfer of masses (in russian). In *Doklady Akademii Nauk*, volume 37, pages 227–229, 1942.
- Hermann Karcher. Riemannian center of mass and mollifier smoothing. *Communications on pure and applied mathematics*, 30(5):509–541, 1977.
- Hamed Karimi, Julie Nutini, and Mark Schmidt. Linear convergence of gradient and proximal-gradient methods under the polyak-łojasiewicz condition. In *Joint European conference on machine learning and knowledge discovery in databases*, pages 795–811. Springer, 2016.
- Sirvan Khalighi, Teresa Sousa, Gabriel Pires, and Urbano Nunes. Automatic sleep staging: A computer assisted approach for optimal combination of features and polysomnographic channels. *Expert Systems with Applications*, 40(17):7046–7059, 2013.
- Benoît Kloeckner. A geometric study of wasserstein spaces: Euclidean spaces. *Annali della Scuola Normale Superiore di Pisa-Classe di Scienze*, 9(2):297–323, 2010.
- Ivan Kobyzev, Simon JD Prince, and Marcus A Brubaker. Normalizing flows: An introduction and review of current methods. *IEEE transactions on pattern analysis and machine intelligence*, 43(11):3964–3979, 2020.
- Alexander Kolesov, Petr Mokrov, Igor Udovichenko, Milena Gazdieva, Gudmund Pammer, Evgeny Burnaev, and Alexander Korotin. Estimating barycenters of distributions with neural optimal transport. *arXiv preprint arXiv:2402.03828*, 2024.
- Alexander Korotin, Lingxiao Li, Justin Solomon, and Evgeny Burnaev. Continuous wasserstein-2 barycenter estimation without minimax optimization. *arXiv preprint arXiv:2102.01752*, 2021.
- Alexander Korotin, Vage Egiazarian, Lingxiao Li, and Evgeny Burnaev. Wasserstein iterative networks for barycenter estimation. *Advances in Neural Information Processing Systems*, 35:15672–15686, 2022a.
- Alexander Korotin, Daniil Selikhanovych, and Evgeny Burnaev. Neural optimal transport. *arXiv preprint arXiv:2201.12220*, 2022b.
- Wouter M Kouw and Marco Loog. A review of domain adaptation without target labels. *IEEE transactions on pattern analysis and machine intelligence*, 43(3):766–785, 2019.
- Matthias Liero, Alexander Mielke, and Giuseppe Savaré. Optimal entropy-transport problems and a new hellinger-kantorovich distance between positive measures. *Inventiones mathematicae*, 211(3):969–1117, 2018.
- Laurens van der Maaten and Geoffrey Hinton. Visualizing data using t-sne. *Journal of machine learning research*, 9 (Nov):2579–2605, 2008.
- Ashok Makkuva, Amirhossein Taghvaei, Sewoong Oh, and Jason Lee. Optimal transport mapping via input convex neural networks. In *International Conference on Machine Learning*, pages 6672–6681. PMLR, 2020.
- Gaspard Monge. Mémoire sur la théorie des déblais et des remblais. *Histoire de l'Académie Royale des Sciences de Paris*, 1781.
- Eduardo Montesuma, Fred Maurice Ngole Mboula, and Antoine Souloumiac. Multi-source domain adaptation through dataset dictionary learning in wasserstein space. In *ECAI 2023*, pages 1739–1746. IOS Press, 2023.
- Eduardo Fernandes Montesuma and Fred Maurice Ngole Mboula. Wasserstein barycenter for multi-source domain adaptation. In *Proceedings of the IEEE/CVF conference on computer vision and pattern recognition*, pages 16785–16793, 2021.
- Eduardo Fernandes Montesuma, Fred Ngolè Mboula, and Antoine Souloumiac. Multi-source domain adaptation meets dataset distillation through dataset dictionary learning. In *ICASSP 2024-2024 IEEE International Conference on Acoustics, Speech and Signal Processing (ICASSP)*, pages 5620–5624. IEEE, 2024a.
- Eduardo Fernandes Montesuma, Fred Ngolè Mboula, and Antoine Souloumiac. Lighter, better, faster multi-source domain adaptation with gaussian mixture models and optimal transport. In *Joint European Conference on Machine Learning and Knowledge Discovery in Databases*, pages 21–38. Springer, 2024b.
- Eduardo Fernandes Montesuma, Michela Mulas, Fred Ngolè Mboula, Francesco Corona, and Antoine Souloumiac. Benchmarking domain adaptation for chemical processes on the tennessee eastman process. In *MLACCE Workshop*, 2024c.
- Eduardo Fernandes Montesuma, Fred Maurice Ngolè Mboula, and Antoine Souloumiac. Recent advances in optimal transport for machine learning. *IEEE Transactions on Pattern Analysis and Machine Intelligence*, 47(2): 1161–1180, 2025. doi: 10.1109/TPAMI.2024.3489030.

- Frank Nielsen. An elementary introduction to information geometry. *Entropy*, 22(10), 2020. ISSN 1099-4300. doi: 10.3390/e22101100. URL <https://www.mdpi.com/1099-4300/22/10/1100>.
- Sinno Jialin Pan and Qiang Yang. A survey on transfer learning. *IEEE Transactions on knowledge and data engineering*, 22(10):1345–1359, 2009.
- Gabriel Peyré and Marco Cuturi. Computational optimal transport: With applications to data science. *Foundations and Trends® in Machine Learning*, 11(5-6):355–607, 2019.
- Boris T Polyak. Gradient methods for solving equations and inequalities. *USSR Computational Mathematics and Mathematical Physics*, 4(6):17–32, 1964.
- Léo Portales, Edouard Pauwels, and Elsa Cazelles. Sample complexity of optimal transport barycenters with discrete support. *arXiv preprint arXiv:2505.21274*, 2025.
- Joaquin Quiñero-Candela, Masashi Sugiyama, Anton Schwaighofer, and Neil D Lawrence. *Dataset shift in machine learning*. Mit Press, 2022.
- Ievgen Redko, Nicolas Courty, Rémi Flamary, and Devis Tuia. Optimal transport for multi-source domain adaptation under target shift. In *The 22nd International Conference on artificial intelligence and statistics*, pages 849–858. PMLR, 2019.
- Christopher Reinartz, Murat Kulahci, and Ole Ravn. An extended tennessee eastman simulation dataset for fault-detection and decision support systems. *Computers & chemical engineering*, 149:107281, 2021.
- Tobias Ringwald and Rainer Stiefelhagen. Adaptiope: A modern benchmark for unsupervised domain adaptation. In *Proceedings of the IEEE/CVF winter conference on applications of computer vision*, pages 101–110, 2021.
- Kate Saenko, Brian Kulis, Mario Fritz, and Trevor Darrell. Adapting visual category models to new domains. In *European conference on computer vision*, pages 213–226. Springer, 2010.
- Filippo Santambrogio. *Optimal transport for applied mathematicians*, volume 87. Springer, 2015.
- Filippo Santambrogio. {Euclidean, metric, and Wasserstein} gradient flows: an overview. *Bulletin of Mathematical Sciences*, 7:87–154, 2017.
- Sidak Pal Singh and Martin Jaggi. Model fusion via optimal transport. *Advances in Neural Information Processing Systems*, 33:22045–22055, 2020.
- Richard Sinkhorn. A relationship between arbitrary positive matrices and doubly stochastic matrices. *The annals of mathematical statistics*, 35(2):876–879, 1964.
- Sanvesh Srivastava, Cheng Li, and David B Dunson. Scalable bayes via barycenter in wasserstein space. *Journal of Machine Learning Research*, 19(8):1–35, 2018.
- Shiliang Sun, Honglei Shi, and Yuanbin Wu. A survey of multi-source domain adaptation. *Information Fusion*, 24: 84–92, 2015.
- Asuka Takatsu. Wasserstein geometry of gaussian measures. *Osaka Journal of Mathematics*, 2011.
- Rosanna Turrisi, Rémi Flamary, Alain Rakotomamonjy, and Massimiliano Pontil. Multi-source domain adaptation via weighted joint distributions optimal transport. In *Uncertainty in artificial intelligence*, pages 1970–1980. PMLR, 2022.
- Vladimir N Vapnik. An overview of statistical learning theory. *IEEE transactions on neural networks*, 10(5): 988–999, 1999.
- Hemanth Venkateswara, Jose Eusebio, Shayok Chakraborty, and Sethuraman Panchanathan. Deep hashing network for unsupervised domain adaptation. In *Proceedings of the IEEE Conference on Computer Vision and Pattern Recognition*, pages 5018–5027, 2017.
- Cédric Villani. *Optimal transport: old and new*, volume 338. Springer, 2008.
- Gabriele Visentin and Patrick Cheridito. Computing optimal transport maps and wasserstein barycenters using conditional normalizing flows. *arXiv preprint arXiv:2505.22364*, 2025.
- Jiquan Wang, Sha Zhao, Zhiling Luo, Yangxuan Zhou, Haiteng Jiang, Shijian Li, Tao Li, and Gang Pan. Cbramod: A criss-cross brain foundation model for eeg decoding. *arXiv preprint arXiv:2412.07236*, 2024.
- Jiacheng Zhu, Jieli Qiu, Aritra Guha, Zhuolin Yang, XuanLong Nguyen, Bo Li, and Ding Zhao. Interpolation for robust learning: Data augmentation on wasserstein geodesics. In *International conference on machine learning*, pages 43129–43157. PMLR, 2023.

Wasserstein Gradient Flows for Scalable and Regularized Barycenter Computation

Eduardo Fernandes Montesuma¹

Yassir Bendou¹

Mike Gartrell¹

¹Sigma Nova, Paris, France

CONTENTS

1	Introduction	1
2	Background	2
2.1	Optimal Transport	3
2.2	Wasserstein Barycenter	3
2.3	Gradient Flows	3
3	Wasserstein Barycenters as Gradient Flows	3
3.1	Scaling with Mini-Batch OT	4
3.2	Flows over Joint Measures	5
3.3	Task-Aware Regularizing Functionals	5
3.4	Convergence	5
4	Experiments	6
4.1	Swiss Roll Measures	6
4.2	Multi-Source Domain Adaptation	7
5	Conclusion	8
A	Introduction	13
B	A Brief Survey on Wasserstein Barycenters	13
B.1	Introduction	13
B.2	Discrete Barycenter Solvers	14
B.3	Neural Barycenter Solvers	14
B.4	Future Directions	17

C	Additional Background	18
C.1	Calculus in Wasserstein Spaces	18
C.2	Wasserstein Gradient of Functionals	18
D	Proof of Theorem 3.1	21
D.1	Empirical Verification of the PL Inequality	22
D.2	PL Inequality on Location-Scatter Family	23
E	Domain Adaptation	25
E.1	Introduction	25
E.2	Source-Only Training	25
E.3	Wasserstein Barycenter Transport	25
E.4	Adapting Neural Network Barycenter Solvers to DA	27
F	Additional Experiments	27
F.1	Evaluation Protocol and Backbones	27
F.2	Fine-Grained Results	28
F.3	Complexity Analysis and Additional Running Time	30
F.4	Effect of Different Functionals	31
F.5	Hyperparameter Setting	32
F.6	Ablation	33

A INTRODUCTION

The goal of this supplementary material is to provide additional background on the main paper, as well as to provide missing proofs, additional experiments, and the complete experimental setting. These details were left out of the main paper due to length constraints.

Organization. We divide this supplementary material as follows. Section B provides a brief survey on the methods for computing Wasserstein barycenters. Section C.1 provides additional background on OT. Section C.2 covers additional details on the potential, internal, and interaction energies, as well as the barycenter objectives and their gradients. Section D provides missing proofs. Finally, section F provide additional experiments.

B A BRIEF SURVEY ON WASSERSTEIN BARYCENTERS

B.1 INTRODUCTION

Given a finite family of measures $\mathcal{Q} = \{Q_k\}_{k=1}^K$, the Wasserstein barycenter problem was first introduced by Agueh and Carlier [2011] as the following minimization problem,

$$P^* = \arg \min_{P \in \mathcal{P}_2(\Omega)} \left\{ \mathbb{B}_\epsilon(P|\mathcal{Q}) = \sum_{k=1}^K \lambda_k \mathbb{W}_{2,\epsilon}(P, Q_k)^2 \right\}, \quad (25)$$

where $\epsilon \geq 0$ denotes the entropic regularization weight. This minimization problem is the analogous, in Wasserstein space, to the *Euclidean barycenter* problem $x \mapsto \sum_k \lambda_k d(x, x_k)^2$, which is made possible since $(\mathcal{P}_2(\Omega), \mathbb{W}_2)$ is a metric space. Solving problem 25 is, in general, challenging. Except for the Gaussian case, there are no closed-form solutions. In the following, we review a few strategies for computing Wasserstein barycenters.

B.2 DISCRETE BARYCENTER SOLVERS

Discrete barycenter solvers are based on the empirical approximation of the underlying measures, that is,

$$\hat{P}(z) = \sum_{i=1}^n a_i \delta(z - z_i^{(P)}) \in \text{Emp}_n(\Omega). \quad (26)$$

Here, $\{z_i^{(P)}\}_{i=1}^n$ is the support of \hat{P} and $a = \{a_i : a_i \geq 0, \text{ and } \sum a_i\}_{i=1}^n$ are the sample weights. There are two prevalent strategies when discretizing P . First, one can fix a grid/bins over the underlying space Ω , and compute $a_i = P(z_i^{(P)})$ as the bin weight. This strategy is equivalent to estimating the density of P over Ω . Second, we can sample $z_i^{(P)}$ i.i.d. P , in which case $a_i = 1/n$. In this paper, we deal primarily with *free-support* Wasserstein barycenters. Arguably, the first free-support algorithm was proposed by Cuturi and Doucet [2014]. Their strategy comes from plugging equation 26 into 25,

$$\begin{aligned} Z^{(P),*} &= \arg \min_{z_1^{(P)}, \dots, z_n^{(P)} \in \Omega} \left\{ \mathbb{B}_\epsilon(P|Q) = \sum_{k=1}^K \lambda_k \sum_{i=1}^n \sum_{j=1}^{n_k} \gamma_{\epsilon,k,i,j} \|z_i^{(P)} - z_j^{(Q_k)}\|_2^2 \right\}, \\ \text{subject to } \gamma_{\epsilon,k}^* &= \arg \min_{\gamma \in \Gamma(P, Q_k)} \sum_{i=1}^n \sum_{j=1}^{n_k} \gamma_{ij} \|z_i^{(P)} - z_j^{(Q_k)}\|_2^2 + \epsilon \sum_{i=1}^n \sum_{j=1}^{n_k} \gamma_{ij} \log \gamma_{ij} \end{aligned} \quad (27)$$

At this point, one should compare equation 27 with equation 18 in the main paper. Cuturi and Doucet [2014] propose solving this equation via a block coordinate descent strategy. Indeed, assume $\gamma_k = \text{OT}(P, Q_k)$ has been calculated (e.g., through linear programming), then,

$$\nabla_{z_i^{(P)}} \mathbb{B}_\epsilon(P|Q) = 2 \sum_{k=1}^K \lambda_k \sum_{j=1}^{n_k} \gamma_{k,i,j} (z_i^{(P)} - z_j^{(Q_k)}) = \frac{2}{n} z_i^{(P)} - 2 \sum_{k=1}^K \lambda_k \sum_{j=1}^{n_k} \gamma_{k,i,j} z_j^{(Q_k)}.$$

As a consequence, $\nabla_{z_i^{(P)}} \mathbb{B}_\epsilon(P|Q) = 0$ leads to an update rule in terms of the barycentric projection of P to Q_k , which is a discrete approximation of the Monge map Deb et al. [2021].

An important question comes when the samples from P are feature-label joints, first raised by Montesuma et al. [2023], who proposed to use the ground-cost,

$$d(z, z') = \sqrt{\|x - x'\|_2^2 + \beta \|y - y'\|_2^2}, \quad (28)$$

where y and y' are one-hot encoded labels, and $\beta \geq 0$ strikes a balance between the features and labels terms. As we show in the main paper, since this ground-cost is a metric, computing the OT cost with d^2 as the ground-cost is equivalent to computing the 2-Wasserstein distance on $\mathcal{X} \times \mathcal{Y}$.

The first paper to remark these computations was Montesuma et al. [2023], who proposed to couple these mappings,

$$x_{\tau+1,i}^{(P)} = \sum_{k=1}^K \lambda_k \underbrace{\left(n \sum_{i=1}^n \sum_{j=1}^{n_k} \gamma_{k,i,j} x_j^{(Q_k)} \right)}_{T_{P \rightarrow Q_k}^*(x_{\tau,i}^{(P)})}, \text{ and, } y_{\tau+1,i}^{(P)} = \sum_{k=1}^K \lambda_k \underbrace{\left(n \sum_{i=1}^n \sum_{j=1}^{n_k} \gamma_{k,i,j} y_j^{(Q_k)} \right)}_{T_{P \rightarrow Q_k}^*(y_{\tau,i}^{(P)})}. \quad (29)$$

These iterations have a few nice properties with respect to the label term. First, the mappings $T_{P \rightarrow Q_k}^*(y_{i,\tau}^{(P)})$ correspond to label propagation terms first defined in Redko et al. [2019]. Second, since the summations in equation 29 are convex combinations of the labels, the update rules naturally suffice $y_{\tau,i}^{(P)} \in \Delta_{n_{\text{classes}}}$. Third, these iterations can be understood as *fixed-point iterations* in the sense of Álvarez-Esteban et al. [2016]. The authors use this algorithm as the building block of their dictionary learning strategy.

B.3 NEURAL BARYCENTER SOLVERS

In this section, we cover a collection of methods that use neural networks as the foundation of computing Wasserstein barycenters. These methods are oftentimes referred to as "continuous", thus relying on the idea that the calculated barycenter

is a continuous measure. Note that this is different than claiming that these barycenters solve a *continuous problem*. In fact, most methods are formulated in terms of expectations of the involved measures, which are approximated through mini-batching. Indeed, mini-batching is the main tool for scalability in Wasserstein barycenters.

Generative Modeling. One of the first methods was proposed by Cohen et al. [2020], who proposed viewing equation 25 through the lens of generative modeling. Let g_θ denote a neural network with parameters θ . Then,

$$\theta^* = \arg \min_{\theta \in \Theta} \sum_{k=1}^K \lambda_k \mathbb{W}_2(P_\theta, Q_k)^2,$$

where $P_\theta = g_{\theta, \#} P_0$ is the push-forward of a latent measure P_0 by the generator g_θ . Therefore, the Wasserstein barycenter is parametrized via the weights of g_θ . In comparison, methods such as Cuturi and Doucet [2014] and Montesuma et al. [2023] parametrize the barycenter through its samples. The underlying idea is sampling from each Q_k and $P_0 = \mathcal{N}(0, \sigma^2 I)$.

Input Convex Neural Nets. More refined settings exploit the properties of the 2-Wasserstein distance with the squared Euclidean ground-cost. Indeed, from [Makkuva et al., 2020, Equation 4], exploiting the decomposition

$$\|z - z'\|_2^2 = \|z\|_2^2 + \|z'\|_2^2 - 2\langle z, z'\rangle,$$

we can obtain,

$$\frac{1}{2} \mathbb{W}_2(P, Q)^2 = \underbrace{\int \frac{\|z\|_2^2}{2} dP(z) + \int \frac{\|z\|_2^2}{2} dQ(z)}_{\mathcal{C}(P, Q)} - \min_{f, g \in \Phi} \int f(z) dP(z) + \int g(z) dQ(z), \quad (30)$$

where $(f, g) \in \Phi = \{f(x) + g(y) \leq \|x - y\|_2^2\}$ are called potentials. The main insight of Makkuva et al. [2020] is rewriting the minimization problem in the r.h.s. of equation 30 as,

$$\sup_{f \in \text{CVX}} \inf_{g \in \text{CVX}} \underbrace{- \int f(z) dP(z) - \int (\langle z, \nabla g(z) \rangle - f(\nabla g(z))) dQ(z)}_{V_{P, Q}(f, g)}$$

Based on these equations, Fan et al. [2020] propose solving,

$$(h, \{f_k\}_{k=1}^K, \{g_k\}_{k=1}^K) = \min_h \sup_{f_k \in \text{CVX}} \inf_{g_k \in \text{CVX}} \frac{1}{2} \int \|h(z)\|_2^2 dP_0(z) + \sum_{k=1}^K \lambda_k V_{P, Q_k}(f_k, g_k). \quad (31)$$

Here, samples in the Wasserstein barycenter are generated through the forward pass $h(z)$, where $z \sim P_0 = \mathcal{N}(0, \sigma^2 I)$. This is a min-max-min problem, which, as with many problems involving neural nets (e.g., generative adversarial nets [Goodfellow et al., 2014]), is subject to saddle points.

An important aspect of equation 31 is the minimization with respect convex functions f_k and g_k . Indeed, these are the potentials of the transportation problem between the barycenter P and each Q_k . More specifically, In light of Brenier's theorem Brenier [1991], ∇g_k is the Monge map from Q_k to the barycenter P . These elements motivate Fan et al. [2020] using Input Convex Neural Networks (ICNNs), as in Makkuva et al. [2020], for the optimization problem in equation 31.

Continuous 2-Wasserstein Barycenter. We now cover a family of methods relying on the fixed-point view of Wasserstein barycenters introduced by Álvarez-Esteban et al. [2016]. Indeed, these authors show that the Wasserstein barycenter is a fixed point of the operator $\Psi : P \mapsto (\sum_k \lambda_k T_{P \rightarrow Q_k})_{\#} P$. This is actually the principle behind most of the discrete methods described in the previous section. Now, with respect to OT potentials, if $\Psi(P) = P$, then one has,

$$\sum_{k=1}^K \lambda_k T_{Q_k \rightarrow P}^*(z) = z \xrightarrow{(a)} \sum_{k=1}^K \lambda_k \nabla g_k(z) = z \xrightarrow{(b)} \sum_{k=1}^K \lambda_k g_k(z) = \frac{\|z\|_2^2}{2} + c$$

where implication (a) follows from Brenier's theorem, and g_k is the potential of the transportation problem from Q_k to P , and implication (b) follows by integration. Here, since c is an integration constant, one can conveniently take $c = 0$. Now, denote $\text{Congruent}(\lambda) = \{g_{1:K} = (g_1, \dots, g_K) : \sum_k \lambda_k g_k(z) = \|z\|_2^2/2\}$ be the set of congruent potentials $g_{1:K} = (g_1, \dots, g_K)$

with respect to coordinates λ . Using the dual formulation in equation 30 and restricting the set of potentials to congruent potentials,

$$\mathbb{B}(P|Q) = \sum_{k=1}^K \lambda_k \mathbb{E}_{z \sim Q_k} \left[\frac{\|z\|_2^2}{2} \right] + \mathbb{E}_{z \sim P} \left[\frac{\|z\|_2^2}{2} \right] - \min_{g_{1:K} \in \text{Congruent}(\lambda)} \left(\sum_{k=1}^K \lambda_k (\mathbb{E}_{z \sim Q_k} [f_k(z)] + \mathbb{E}_{z \sim P} [g_k](z)) \right),$$

where $g_{1:K} = (g_1, \dots, g_K)$. Now, taking the expectation on the congruence constraint, we have,

$$\sum_{k=1}^K \lambda_k \mathbb{E}_{z \sim P} [g_k(z)] = \mathbb{E}_{z \sim P} \left[\frac{\|z\|_2^2}{2} \right],$$

which allowed Korotin et al. [2021] to simplify $\mathbb{B}(P|Q)$ into,

$$\mathbb{B}(P|Q) = \sum_{k=1}^K \lambda_k \mathbb{E}_{z \sim Q_k} \left[\frac{\|z\|_2^2}{2} \right] - \min_{g_{1:K} \in \text{Congruent}(\lambda)} \sum_{k=1}^K \lambda_k \mathbb{E}_{z \sim Q_k} [g_k(z)], \quad (32)$$

which does not involve terms with respect to the barycentric measure P . While the approach of Korotin et al. [2021] simplifies the barycenter objective to expectations with respect to the known measures Q_k , it introduces a challenging constraint – the congruence of potentials. This constraint is challenging, as it is a functional inequality over the whole space Ω . Furthermore, it adds to the already constrained setting of fitting convex functions. Korotin et al. [2021] proposes solving it *approximately*, by penalizing potentials that do not meet the congruence condition. There is a circular dependence here, as one needs an estimate of the Wasserstein barycenter to estimate the constraint violation.

Neural (Weak) Optimal Transport. Weak OT Gozlan et al. [2017], Backhoff-Veraguas et al. [2019] comes from the interpretation of the Kantorovich formulation as,

$$\gamma^* = \arg \inf_{\gamma \in \Gamma(P, Q)} \int_{\Omega} C(z, \gamma(\cdot|z)) dP(z), \text{ where, } C(z, Q) = \int_{\Omega} c(z, z') dQ(z'), \quad (33)$$

this formulation allows for more general costs $C : \Omega \times \mathcal{P}(\Omega) \rightarrow \mathbb{R}$, i.e., costs that take a sample and a probability measure as inputs. In this sense, Kolesov et al. [2024] extends equation 32 to,

$$\mathbb{B}(P|Q) = \sum_{k=1}^K \lambda_k \left(\mathbb{E}_{z \sim Q_k} [C_k(z, \gamma(\cdot|z))] - \mathbb{E}_{z \sim Q_k} [\mathbb{E}_{z' \sim \gamma(\cdot|z)} (g_k(z'))] \right), \quad (34)$$

which holds for congruent potentials $\sum_k \lambda_k g_k = 0$. As with equation 32, \mathbb{B} does not depend explicitly on the unknown barycentric measure P . As such, the authors compute the barycenter through a max-min optimization problem,

$$\max_{\{g_{1:K} : \sum_k \lambda_k g_k = 0\}} \min_{\{\gamma_1, \dots, \gamma_K : \gamma_k(\cdot|z) \in \Gamma(P_k)\}} \left\{ \sum_{k=1}^K \lambda_k \left(\mathbb{E}_{z \sim Q_k} [C_k(z, \gamma_k(\cdot|z))] - \mathbb{E}_{z \sim Q_k} [\mathbb{E}_{z' \sim \gamma_k(\cdot|z)} (g_k(z'))] \right) \right\}.$$

This extension opens up new possibilities for weak OT barycenters. For instance,

$$C_{\text{classical}}(x, \gamma) = \frac{1}{n} \sum_{j=1}^n c(z_i^{(P)}, z_j^{(Q)}) \quad C_{\text{KL}}(x, \gamma) = \frac{1}{n} \sum_{j=1}^n c(z_i^{(P)}, z_j^{(Q)}) + \epsilon \text{KL}(\mathcal{N}(\mu(z), \sigma(z)) | P_0),$$

where $C_{\text{classical}}$ allows us to retrieve the original OT problem. C_{KL} is an alternative, when modeling $\gamma(\cdot|z) = \mathcal{N}(\mu(z), \sigma(z))$. On top of this reformulation, the authors in Kolesov et al. [2024] propose approximating $\gamma(\cdot|z)$ through a mapping, as in Korotin et al. [2022b], that is,

$$\gamma(\cdot|z) = T(z, s), \text{ subject to } s \sim \mathbb{S},$$

where \mathbb{S} is some prior measure, such as $\mathbb{S} = \mathcal{N}(0, I)$. In this context, Gazdieva et al. [2024] extends this idea in the semi-unbalanced OT setting Liero et al. [2018], where one of the mass preservation constraint of one of the marginals of γ is relaxed. More specifically, given $\xi : \mathbb{R}_+ \rightarrow \mathbb{R}_+$,

$$D_{\xi}(P||Q) = \int_{\Omega} \xi \left(\frac{P(z)}{Q(z)} \right) dQ(z) \text{ if } P \ll Q \text{ and } +\infty \text{ otherwise,}$$

where $P \ll Q$ means that P is absolutely continuous with respect to Q . We denote $\bar{\xi}(z') = \sup_{z \in \mathbb{R}} \{zz' - \xi(z)\}$ to be its convex conjugate. With that in mind, Gazdieva et al. [2024] shows, in Theorem 1 and Corollaries 1 and 2, that minimizing,

$$\arg \min_{P \in \mathcal{P}_2} \sum_{k=1}^K \lambda_k \left(\int_{\Omega} \int_{\Omega} c(z, z') d\gamma(z, z') + D_{\xi}(\gamma(\cdot|\cdot) \| Q_k) \right),$$

is equivalent to the following max-min problem,

$$\max_{\{g_{1:K}: \sum_k \lambda_k g_k = 0\}} \min_{\{\gamma_1, \dots, \gamma_K: \gamma_k(\cdot|z) \in \Gamma(P_k)\}} \left\{ \sum_{k=1}^K \lambda_k \left(\mathbb{E}_{z \sim Q_k} \left[-\bar{\xi}_k \left(-\mathbb{E}_{z' \sim \gamma_k(\cdot|z)} [c_k(z, z') - g_k(z')] \right) \right] \right) \right\}.$$

Normalizing Flows. This approach was proposed by Visentin and Cheridito [2025], and relies on the analysis of Gangbo and McCann [1996]. Their main idea is re-writing the Wasserstein distance in terms of functions f, g ,

$$\mathbb{W}_2(P, Q)^2 = \inf_{f \in \text{Borel}(P_0, P), g \in \text{Borel}(P_0, Q)} \|f - g\|_{L_2(P_0)}^2, \quad (35)$$

where $\text{Borel}(P, Q)$ is the set of Borel functions such that $f_{\#}P = Q$. Naturally, a solution (f^*, g^*) to the previous problem gives the transport map $T = g^* \circ f^{-1}$, where f^{-1} is the inverse of f^* . Furthermore, P_0 is an arbitrary latent measure, which further links the approach with generative modeling (i.e., take $P_0 = \mathcal{N}(0, \mathbf{I})$).

Based on equation 35, the insight of Visentin and Cheridito [2025] is modeling f and g through a conditional function $f(z, s)$, $s \in \{0, 1\}$. The Wasserstein barycenter problem is a straightforward generalization of the 2 measures case. For instance, the authors consider $S = \{1, \dots, K\}$, which means that,

$$\mathbb{B}(P|Q) = \sum_{k=1}^K \lambda_k \mathbb{W}_2(P, Q_k)^2 = \sum_{k=1}^K \lambda_k \mathbb{W}_2(g_{\#}P_0, Q_k)^2 = \sum_{k=1}^K \lambda_k \|g - f(z, k)\|_{L_p(P_0)}^2,$$

where g is the push-forward of P_0 to the barycenter P^* , and $f(z, k)$ is the push-forward of Q_k to P^* . As the authors show in [Visentin and Cheridito, 2025, Theorem 3.3],

$$g(z) = \sum_{k=1}^K \lambda_k f(z, k).$$

The main challenge in Visentin and Cheridito [2025] is formulating a conditional model $f: \Omega \times S$. As the authors discuss, one possibility would be using $K = |S|$ different neural nets for modeling $f(z, \cdot)$, which is similar to what is done, for instance, in the neural net methods. The authors take a different route and use conditional normalizing flows Kobyzev et al. [2020] to model these functions.

B.4 FUTURE DIRECTIONS

From the previous discussion on neural net-based methods for computing Wasserstein barycenters, we can identify a few common design choices. For instance, Korotin et al. [2021], Kolesov et al. [2024] and Gazdieva et al. [2024] use $\mathcal{O}(K)$ neural nets for computing Wasserstein barycenters. This design choice results in a parametrization of the underlying barycenter that grows with the number of input measures. The only neural net-based method that differs from this idea is Visentin and Cheridito [2025], which uses a conditional model $f: \Omega \times S$.

Meanwhile, as we cover in our experiments (C.f., Section 4 in the main paper), there is a clear advantage of incorporating labels in the ground-cost when these are available. Unfortunately, it is not clear how to integrate label information in the existing methods. For instance, one could consider using the continuous parametrization in terms of logits ℓ , as we described in Section 3.3. However, there are a few caveats,

1. Normalizing flows require invertible transformations. However, the softmax operation for getting the labels, i.e., $y = \text{softmax}(\ell)$, is not invertible.
2. Using ICNNs, one can enforce the convexity of $z = (x, \ell)$. However, applying the softmax breaks the convexity requirement.

As a result, adapting neural net based methods for the joint $\mathcal{X} \times \mathcal{Y}$ space is challenging and not straightforward. We leave this question for future work.

C ADDITIONAL BACKGROUND

C.1 CALCULUS IN WASSERSTEIN SPACES

In this section, we consider $\Omega = \mathbb{R}^d$, $d(z, z') = \|z - z'\|_2$ and $p = 2$ fixed. While our algorithm is more general than this setting, we use these restrictions as they are the most analyzed by current literature. We leave the theoretical results for general metrics and p to future work.

Notation. For the following theoretical analysis, we use the following notation. Given a measurable map $f, g : \Omega \rightarrow \Omega$. Given a measure $P \in \mathcal{P}_2(\Omega)$, we denote,

$$\|f\|_{L_2(P)}^2 = \int_{\Omega} \|f(x)\|_2^2 dP(x).$$

Likewise, we have a notion of inner product,

$$\langle f, g \rangle_P = \int_{\Omega} \langle f(x), g(x) \rangle_{\Omega} dP(x).$$

Definition C.1. Given a functional $\mathbb{F} : \mathcal{P}_2(\Omega)(\mathbb{R}^d) \rightarrow \mathbb{R}$, we call $\delta\mathbb{F}(P) : \mathbb{R}^d \rightarrow \mathbb{R}$, if it exists, the unique (up to additive constants) function such that

$$\left. \frac{d}{d\varepsilon} \mathbb{F}(P + \varepsilon\chi) \right|_{\varepsilon=0} = \int \delta\mathbb{F}(P) d\chi, \quad (36)$$

for every perturbation χ such that, at least for $\varepsilon \in [0, \varepsilon_0]$, the measure $P + \varepsilon\chi \in \mathcal{P}_2(\mathbb{R}^d)$. This functional is called the first variation of \mathbb{F} at P .

We refer readers to [Chewi et al., 2024, Chapter 5] and [Ambrosio et al., 2008, Chapter 8] for further details on gradient flows in Wasserstein spaces. The main tool we will use here is the continuity equation,

$$\partial_t P_t = -\operatorname{div}(P_t v_t),$$

where the divergence operator should be understood in the measure theoretic sense. Here, $v_t : \Omega \rightarrow \Omega$ is a vector field. Now, given $\mathbb{F} : \mathcal{P}_2(\Omega) \rightarrow \mathbb{R}$ with first variation $\delta\mathbb{F}(P) : \Omega \rightarrow \mathbb{R}$, the time derivative of \mathbb{F} along the curve $\{P_t\}_{t \geq 0}$ can be computed as,

$$\partial_t \mathbb{F}(P_t) \stackrel{(1)}{=} \int \delta\mathbb{F}(P_t) d(\partial_t P_t) \stackrel{(2)}{=} - \int \delta\mathbb{F}(P_t) \operatorname{div}(P_t v_t) dz \stackrel{(3)}{=} \int \langle \nabla \delta\mathbb{F}(P_t), v_t \rangle dP_t \stackrel{(4)}{=} \langle \nabla \delta\mathbb{F}(P_t), v_t \rangle_{P_t},$$

where (1) is obtained by taking $\chi = \partial_t P_t$ in equation 36; (2) is obtained by applying the continuity equation; (3) is obtained by using integration by parts; finally, (4) is obtained via the definition of inner product. This motivates the equality,

$$\nabla_W \mathbb{F}(P) = \nabla \delta\mathbb{F}(P). \quad (37)$$

We refer readers to [Chewi et al., 2024, Proposition 5.10], for a more formal derivation. This discussion characterizes the Wasserstein gradient $\nabla_W \mathbb{F}(P) : \Omega \rightarrow \Omega$ as a vector field. Therefore, taking the direction of steepest descent of the functional \mathbb{F} , $v_t = -\nabla_W \mathbb{F}(P_t)$, leads to the following connection between $\partial_t \mathbb{F}(P_t)$ and $\nabla_W \mathbb{F}(P_t)$,

$$\partial_t \mathbb{F}(P_t) = -\|\nabla_W \mathbb{F}(P_t)\|_{L_2(P_t)}^2, \quad (38)$$

C.2 WASSERSTEIN GRADIENT OF FUNCTIONALS

In this section, we give an overview on the Wasserstein gradient of the terms used in equation 16. We refer readers to [Chewi et al., 2024, Chapter 5] and [Santambrogio, 2017, Section 4] for further details.

Potential Energy, \mathbb{V} . For reference, this functional corresponds to,

$$\mathbb{V}(P) = \mathbb{E}_{z \sim P}[V(z)] = \int V(z) dP(z),$$

for some potential function $V : \Omega \rightarrow \mathbb{R}$. From the definition of first variation,

$$\mathbb{V}(P + \epsilon\chi) = \int V(z)dP(z) + \epsilon \int V(z)d\chi(z),$$

then, taking the derivative with respect to ϵ ,

$$\frac{d}{d\epsilon}\mathbb{V}(P + \epsilon\chi) = \int V(z)d\chi,$$

which means that $V = \delta\mathbb{V}(P)$. As a consequence, the Wasserstein gradient of \mathbb{V} is,

$$\nabla_W\mathbb{V} = \nabla V.$$

which is a vector field over Ω . Since \mathbb{V} is linear in P , it is convex. Furthermore, its continuity with respect to the weak convergence depends on the regularity of V . For instance, if V is bounded, \mathbb{V} is continuous. If V is lower semi-continuous and bounded from below, then \mathbb{V} is semi-continuous.

Internal Energy, \mathbb{G} . The internal energy takes the form,

$$\mathbb{G}(P) = \int G(P(z))dz,$$

where $P(z)$ is understood as the density of the measure P , with respect the Lebesgue measure. Let us assume χ admits a density with respect the Lebesgue measure as well. In this case,

$$\mathbb{G}(P + \epsilon\chi) = \int G(P(z) + \epsilon\chi(z))dz.$$

Taking the derivative under the integral sign,

$$\left. \frac{d}{d\epsilon}\mathbb{G}(P + \epsilon\chi) \right|_{\epsilon=0} = \int G'(P(z))\chi(z)dz = \int G'(P(z))d\chi(z),$$

which means that $\delta\mathbb{G} = G'(P)$ and $\nabla_W\mathbb{G} = \nabla G'(P(z))$.

Interaction Energy, \mathbb{U} . Here, let us assume $U(z, z')$ symmetric for simplicity,

$$\mathbb{U}(P) = \int \int U(z, z')dP(z)dP(z'),$$

hence,

$$\mathbb{U}(P + \epsilon\chi) = \int \int U(z, z')dP(z)dP(z') + 2\epsilon \int \int U(z, z')dP(z)d\chi(z') + \mathcal{O}(\epsilon^2).$$

Again, taking derivatives with respect ϵ ,

$$\left. \frac{d}{d\epsilon}\mathbb{U}(P + \epsilon\chi) \right|_{\epsilon=0} = 2 \int \left(\int U(z, z')dP(z) \right) d\chi(z'),$$

which means that,

$$\delta\mathbb{U}(P) = 2 \int U(z, z')dP(z).$$

When $U(z, z') = h(z - z')$ for an even h , $\int U(z, z')dP(z) = \int h(z - z')P(z)dz = h \star P$, i.e., the convolution of h and P . Furthermore, $\nabla_W\mathbb{U} = (\nabla h) \star P$

Barycenter Functional, \mathbb{B} . For the barycenter functional, we can derive its first variation from the 2–Wasserstein distance. Assume there exists an OT map $T_{P \rightarrow Q}^*$. In this case,

$$\nabla_W\mathbb{W}_2(P, Q)^2 = 2(\text{Id} - T_{P \rightarrow Q}^*). \quad (39)$$

Therefore, given $\mathcal{Q} = \{Q_1, \dots, Q_K\}$, it is straightforward to obtain:

$$\nabla_W \mathbb{B}(P|\mathcal{Q}) = \nabla_W \left(\sum_{k=1}^K \lambda_k \mathbb{W}_2(P, Q_k)^2 \right) = 2 \sum_{k=1}^K \lambda_k (\text{Id} - T_{P \rightarrow Q_k}^*). \quad (40)$$

A Connection with [Cuturi and Doucet, 2014, Algorithm 2]. Let us now focus on the empirical case with an Euclidean ground-cost. Assume γ^* computed between \hat{P} and \hat{Q} , which means that,

$$\mathbb{W}_2(\hat{P}, \hat{Q})^2 = \sum_{i=1}^n \sum_{j=1}^m \gamma_{ij}^* \|z_i^{(P)} - z_j^{(Q)}\|_2^2, \text{ and } \mathbb{B}(\hat{P}_\tau|\mathcal{Q}) = \sum_{k=1}^K \lambda_k \sum_{i=1}^n \sum_{j=1}^{n_k} \gamma_{k,i,j}^* \|z_{\tau,i}^{(P)} - z_j^{(Q_k)}\|_2^2.$$

We can compute the Wasserstein gradient $\nabla_W \mathbb{B}$ by computing $\nabla_{z_{\tau,i}^{(P)}} \mathbb{B}$, that is,

$$\nabla_{z_{\tau,i}^{(P)}} \mathbb{B}(\hat{P}_\tau|\mathcal{Q}) = 2 \sum_{k=1}^K \lambda_k \sum_{j=1}^{n_k} \gamma_{k,i,j}^* (z_{\tau,i}^{(P)} - z_j^{(Q_k)}) = \frac{2}{n} z_{\tau,i}^{(P)} - 2 \sum_{k=1}^K \lambda_k \sum_{j=1}^{n_k} \gamma_{k,i,j}^* z_j^{(Q_k)}.$$

From this last equation, we can use the barycentric mapping definition,

$$T_{P \rightarrow Q_k}^*(z_{i,\tau}^P) = n \sum_{j=1}^{n_k} \gamma_{k,i,j}^* z_j^{(Q_k)}, \quad (41)$$

to write,

$$\nabla_{z_{\tau,i}^{(P)}} \mathbb{B}(\hat{P}_\tau|\mathcal{Q}) = \frac{2}{n} \left(z_{\tau,i}^{(P)} - \sum_{k=1}^K \lambda_k T_{P \rightarrow Q_k}^*(z_{\tau,i}^{(P)}) \right),$$

which means we can write the gradient flow update rule as,

$$z_{\tau+1,i}^{(P)} = \left(1 - \frac{2\alpha}{n} \right) z_{i,\tau}^{(P)} + \frac{2\alpha}{n} \sum_{k=1}^K \lambda_k T_{P \rightarrow Q_k}^*(z_{i,\tau}^{(P)}),$$

Which is the update rule in [Cuturi and Doucet, 2014, Algorithm 2] with $\theta = 2\alpha/n$. Furthermore, we can also instantiate the fixed-point algorithm of Montesuma et al. [2023], for $\alpha = n/2$. We now highlight two differences of our work with respect these two strategies. First, our setting is more general. In fact, our algorithm is capable of handling ground metrics other than the squared Euclidean metric. Furthermore, our framework couples the barycenter objective with other functionals. Second, while Cuturi and Doucet [2014] assume that *all samples* of $\mathcal{Q} = \{Q_1, \dots, Q_K\}$ are available at once, our algorithm assumes that these measures are available through sampling. This treatment is oftentimes called *continuous* in the literature Korotin et al. [2021, 2022a], however, one still relies on samples from these measures rather than some truly continuous form.

D PROOF OF THEOREM 3.1

In this section, we present the proof for theorem 3.1. We mainly use two tools to obtain this result,

1. The exponential convergence given by the PL inequality,

$$\|\nabla_W \mathbb{B}(P)\|_{L_2(P)}^2 \geq C_{\text{PL}}(\mathbb{B}(P) - \mathbb{B}^*), \quad (42)$$

2. An uniform bound on $P \mapsto \mathbb{B}(P|\mathcal{Q})$ controlling the error of approximating Q_k with \hat{Q}_k .

These results are available, respectively, in Chewi et al. [2024] and Portales et al. [2025]. For completeness, we re-state and demonstrate them. We start with a modified version of [Chewi et al., 2024, Corollary 5.17],

Proposition D.1. (Measure theoretic Gronwall's Lemma Chewi et al. [2024]) Let $\mathbb{F} : \mathcal{P}_2(\Omega) \rightarrow \mathbb{R}$ be a functional that satisfies the PL inequality (c.f. 42) with constant $C_{\text{PL}} > 0$, then,

$$\mathbb{F}(P_\tau) - \mathbb{F}^* \leq e^{-2C_{\text{PL}}\tau} (\mathbb{F}(P_0) - \mathbb{F}^*). \quad (43)$$

Proof. Define $\phi(t) = \mathbb{F}(P_t) - \mathbb{F}^*$. Then,

$$\begin{aligned} \partial_t \phi(t) &= \partial_t \mathbb{F}(P_t) = -\|\nabla_W \mathbb{F}(P_t)\|_{L_2(P_t)}^2, \\ &\geq -C_{\text{PL}}(\mathbb{F}(P_0) - \mathbb{F}^*) = -C_{\text{PL}}\phi(t). \end{aligned}$$

From Grönwall's Lemma [Chewi et al., 2024, Lemma 5.16],

$$\underbrace{\mathbb{F}(P_t) - \mathbb{F}^*}_{\partial_t \phi(t)} \leq e^{-C_{\text{PL}}t} \underbrace{(\mathbb{F}(P_0) - \mathbb{F}^*)}_{\phi(0)}$$

□

We now present the uniform approximation bound of Portales et al. [2025] for empirical barycenters,

Theorem D.1. (Barycenter Empirical Approximation error Portales et al. [2025]) Let $\mathcal{Q} = \{Q_1, \dots, Q_K\}$ be a finite family of measures on $\mathcal{P}_2(\mathcal{B}(0, R))$ for $R > 0$. Approximate each Q_k with m i.i.d. samples $\{z_i^{(Q_k)}\}_{i=1}^m$. Let $\hat{P} = n^{-1} \sum_{i=1}^n \delta_{z_i^{(P)}}$. Let $p \in [1, +\infty)$ and $\epsilon \geq 0$. Then,

$$\mathbb{E} \left[\sup_{z_1^{(P)}, \dots, z_n^{(P)} \in \Omega} |\mathbb{B}_\epsilon(\hat{P}|\mathcal{Q}) - \hat{\mathbb{B}}_\epsilon(\hat{P}|\mathcal{Q})| \right] \leq C_{p,R} \sqrt{\frac{C_{d,n}}{m}}, \quad (44)$$

where,

$$C_{p,R} = \begin{cases} 8\sqrt{2} \int_0^{3(2R)^p} \sqrt{\log\left(2 + \frac{32p(2R)^p}{s}\right)} ds & \epsilon = 0, \\ 8\sqrt{2} \int_0^{(4p+1)(2R)^p} \sqrt{\log\left(2 + \frac{64p(2R)^p}{s}\right)} ds & \epsilon > 0, \end{cases}$$

$$C_{d,n} = n(d+1).$$

With these bounds established, we can then prove our Theorem 3.1.

Proof. Let $\tau > 0$ be the current optimization step. We have the following,

$$\underbrace{\hat{\mathbb{B}}(\hat{P}_\tau) - \hat{\mathbb{B}}^*}_{\text{emp. optimization gap}} = \underbrace{(\hat{\mathbb{B}}(\hat{P}_\tau) - \mathbb{B}(\hat{P}_\tau))}_{\text{emp. approx. gap}} + \underbrace{(\mathbb{B}(\hat{P}_\tau) - \mathbb{B}^*)}_{\text{true optimization gap}} + \underbrace{(\mathbb{B}^* - \hat{\mathbb{B}}^*)}_{\text{emp. approx. gap}}, \quad (45)$$

the optimization gap reflects how far we are from $\inf \mathbb{B}(\hat{P})$ (resp. $\hat{\mathbb{B}}$), whereas the empirical approximation gap reflects the inherent errors of approximating each Q by \hat{Q}_k . In the following we take expectations with respect to samples from Q_k .

From Equation 45 we can bound the expected empirical optimization gap,

$$\mathbb{E}[|\hat{\mathbb{B}}(\hat{P}_\tau) - \hat{\mathbb{B}}^*|] \leq \mathbb{E}[|\hat{\mathbb{B}}(\hat{P}_\tau) - \mathbb{B}(\hat{P}_\tau)|] + \mathbb{E}[|\mathbb{B}(\hat{P}_\tau) - \mathbb{B}^*|] + \mathbb{E}[|\mathbb{B}^* - \hat{\mathbb{B}}^*|]. \quad (46)$$

Now, we can bound the first and third terms using the approximation error of Portales et al. [2025] (i.e., Equation 44),

$$\begin{aligned} \mathbb{E}[|\hat{\mathbb{B}}(\hat{P}_\tau) - \mathbb{B}(\hat{P}_\tau)|] &\leq C_{p,R} \sqrt{\frac{C_{d,n}}{m}}, \\ \mathbb{E}[|\hat{\mathbb{B}}^* - \mathbb{B}^*|] &\leq C_{p,R} \sqrt{\frac{C_{d,n}}{m}}, \end{aligned} \quad (47)$$

here, we recall that $\mathbb{B}^* = \mathbb{B}(P^*) = \inf_P \mathbb{B}(P)$. Returning to the second term, note that the true optimization gap $\mathbb{B}(\hat{P}_\tau | \mathcal{Q}) - \mathbb{B}^*$ is deterministic, as it does not involve sampling from the measures in \mathcal{Q} . This means that,

$$\mathbb{E}[|\mathbb{B}(\hat{P}_\tau) - \mathbb{B}^*|] = |\mathbb{B}(\hat{P}_\tau) - \mathbb{B}^*| \leq e^{-C_{\text{pl}}\tau} (|\hat{\mathbb{B}}(\hat{P}_0) - \hat{\mathbb{B}}^*|). \quad (48)$$

Combining Equations 46, 47 and 48 we get,

$$\mathbb{E}[|\hat{\mathbb{B}}(\hat{P}_\tau) - \hat{\mathbb{B}}^*|] \leq e^{-C_{\text{pl}}\tau} (|\mathbb{B}(\hat{P}_0) - \mathbb{B}^*|) + C_{p,R} \sqrt{\frac{C_{d,n}}{m}},$$

which is the desired inequality. \square

D.1 EMPIRICAL VERIFICATION OF THE PL INEQUALITY

An open question in the literature is the verification of the PL inequality (Equation 42) for general measures, such as empirical ones. To give further context, current results prove that it indeed holds for Gaussian measures, under specific spectral conditions Chewi et al. [2020]. Therefore, we do an empirical validation on whether this bound holds in the empirical case. In a nutshell, to test Equation 42, we need to compute the PL ratio,

$$\text{PL}_{\text{ratio}}(\hat{P}_\tau) = \frac{\|\nabla_W \mathbb{B}(\hat{P}_\tau)\|_{L_2(\hat{P}_\tau)}}{\mathbb{B}(\hat{P}_\tau) - \mathbb{B}^*}, \quad (49)$$

and verify that it indeed remains strictly positive over the course of our optimization. Computing the PL ratio in Equation 49 requires knowledge of \mathbb{B}^* , which is, in general, intractable. However, for location-scatter families, it is known in closed form, since P^* itself is known. Therefore, we verify it in the context of the Swiss-roll measure, where all quantities are known. We show our results in Figure 7, which shows that the ratio converges with iterations to approximately 0.56.

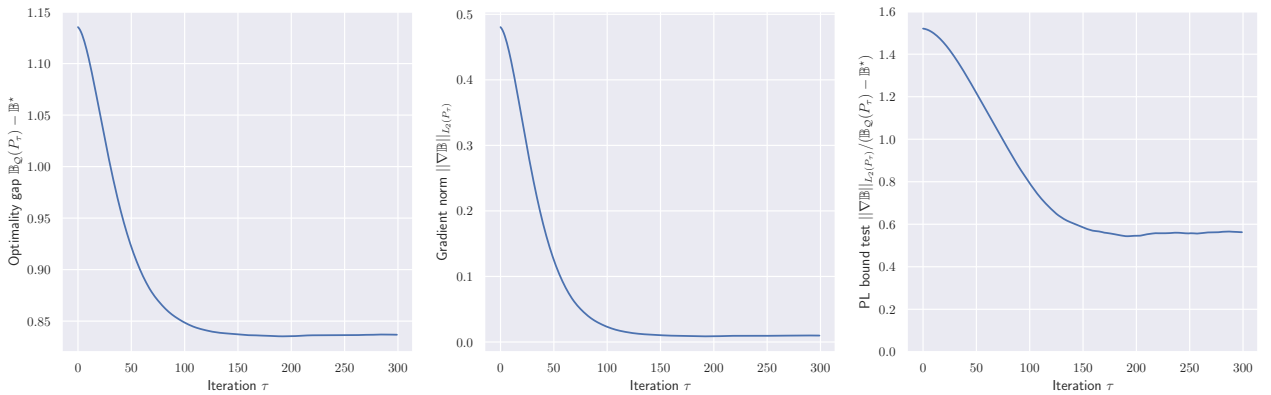


Figure 7: Empirical test of the PL inequality. From left to right, we show: (i) the optimality gap, (ii) the gradient norm, and (iii) the PL ratio as specified in Equation 49.

D.2 PL INEQUALITY ON LOCATION-SCATTER FAMILY

An open question in the literature is the verification of the PL inequality (Equation 42) for general measures. Current results establish that it holds for Gaussian measures under specific spectral conditions [Chewi et al., 2020]. In this section, we show that the PL inequality *transfers* from Gaussians to the broader class of *location-scatter families*, which includes our Swiss roll experiments (Section 4).

Location-Scatter Families. Following Álvarez-Esteban et al. [2016], let $Q_0 \in \mathcal{P}_2(\mathbb{R}^d)$ be a measure with mean μ_0 and covariance Σ_0 . The *location-scatter family* generated by Q_0 is,

$$\mathcal{L}(Q_0) := \{T_{\sharp}Q_0 : T(x) = Ax + m, b \in \mathbb{R}^d, A \in \mathcal{S}_d^{++}\}, \quad (50)$$

where \mathcal{S}_d^{++} denotes the cone of $d \times d$ symmetric positive definite matrices. Each $Q \in \mathcal{L}(Q_0)$ has mean b and covariance A , but inherits the higher-order structure of Q_0 .

Isometry to the Bures-Wasserstein Manifold. The key insight comes from Álvarez-Esteban et al. [2016, Theorem 2.3]: for any $Q_1, Q_2 \in \mathcal{L}(Q_0)$, the 2-Wasserstein distance equals

$$\mathbb{W}_2^2(Q_1, Q_2) = \|\mu_1 - \mu_2\|^2 + \text{Tr}(\Sigma_1 + \Sigma_2 - 2(\Sigma_1^{1/2}\Sigma_2\Sigma_1^{1/2})^{1/2}), \quad (51)$$

This is precisely the Wasserstein distance on the Bures-Wasserstein manifold: $\mathcal{BW} = \{\mathcal{N}(\mu, \Sigma) : \mu \in \mathbb{R}^d, \Sigma \in \mathcal{S}_d^{++}\}$ [Takatsu, 2011]. Henceforth, we note the elements of \mathcal{BW} by $G_{\mu, \Sigma}$. In that sense G_{μ_1, Σ_1} and G_{μ_2, Σ_2} denote the Gaussian measures matching the moments of $Q_1, Q_2 \in \mathcal{L}(Q_0)$. As a consequence, the restriction of \mathbb{W}_2 to $\mathcal{L}(Q_0)$ is *isometric* to the Bures-Wasserstein manifold. Moreover, the optimal transport map between elements of $\mathcal{L}(Q_0)$ takes the same form as for Gaussians:

$$T_{Q_1 \rightarrow Q_2}^*(x) = \mu_2 + A(x - \mu_1), \quad A = \Sigma_1^{-1/2} \left(\Sigma_1^{1/2} \Sigma_2 \Sigma_1^{1/2} \right)^{1/2} \Sigma_1^{-1/2}. \quad (52)$$

Barycenter Functional Equivalence. Let $\mathcal{Q} = \{Q_k\}_{k=1}^K \subset \mathcal{L}(Q_0)$ with $Q_k = T_k Q_0$, such that μ_k and Σ_k are the mean and covariance of Q_k . Let $\mathcal{G} = \{G_{\mu_k, \Sigma_k}\}_{k=1}^K$ be the corresponding Gaussian measures. Equation 51 establishes:

$$\mathbb{B}(P|\mathcal{Q}) = \mathbb{B}(G_{\mu, \Sigma}|\mathcal{G}), \text{ where } P \in \mathcal{L}(Q_0), \text{ and } G_{\mu, \Sigma} \in \mathcal{BW}, \quad (53)$$

where μ, Σ are the mean and covariance of $P \in \mathcal{L}(Q_0)$. Furthermore, by Álvarez-Esteban et al. [2016, Corollary 4.5], the barycenter $P^* \in \mathcal{L}(Q_0)$ corresponds to the Bures-Wasserstein barycenter: if P^* is the minimizer of $P \mapsto \mathbb{B}(P|\mathcal{Q})$ over $\mathcal{L}(Q_0)$ with mean μ^* and covariance Σ^* , then G_{μ^*, Σ^*} is the minimizer of $G_{\mu, \Sigma} \mapsto \mathbb{B}(G_{\mu, \Sigma}|\mathcal{G})$.

Wasserstein Gradient Structure. The Wasserstein gradient of \mathbb{B} at P with mean and covariance μ and Σ is (cf. Equation 40)

$$\nabla_W \mathbb{B}(P|\mathcal{Q}) = 2 \sum_{k=1}^K \lambda_k (\text{Id} - T_{P \rightarrow Q_k}^*). \quad (54)$$

Since each $T_{P \rightarrow Q_k}^*$ is affine (Equation 52), the gradient $\nabla_W \mathbb{B}(P|\mathcal{Q})$ is itself an affine map:

$$\begin{aligned} \nabla_W \mathbb{B}(P|\mathcal{Q})(x) &= 2 \sum_{k=1}^K \lambda_k (x - (A_k x + b_k)), \\ &= 2 \left(x - \left(\sum_{k=1}^K \lambda_k A_k \right) (x) + \sum_{k=1}^K \lambda_k b_k \right), \\ &= \underbrace{\left(2(\text{Id} - \sum_{k=1}^K \lambda_k A_k) \right)}_M (x) + 2 \underbrace{\sum_{k=1}^K \lambda_k b_k}_c, \\ &= Mx + c, \end{aligned} \quad (55)$$

where $M = 2(\text{Id} - \bar{A})$, $c = 2(\bar{A}\mu - \bar{\mu})$, where $\bar{A} = \sum_{k=1}^K \lambda_k A_k$ and $\bar{\mu} = \sum_{k=1}^K \lambda_k \mu_k$. More importantly, by Equation (52), this is *the same affine map* as for the Gaussian case, resulting in,

$$\nabla_W \mathbb{B}(P|\mathcal{Q}) = \nabla_W \mathbb{B}(G_{\mu, \Sigma}|\mathcal{G}) \quad \text{as vector fields } \mathbb{R}^d \rightarrow \mathbb{R}^d. \quad (56)$$

We now establish that the L^2 -norms of these gradients are also equal, which is the key step for transferring the PL inequality.

Lemma D.1 (L^2 -norm of Affine Maps). *Let $T(x) = Mx + c$ be an affine map with $M \in \mathbb{R}^{d \times d}$ and $c \in \mathbb{R}^d$. For any probability measure $P \in \mathcal{P}_2(\mathbb{R}^d)$ with mean μ_P and covariance Σ_P ,*

$$\|T\|_{L^2(P)}^2 := \int_{\mathbb{R}^d} \|T(x)\|^2 dP(x) = \text{Tr}(M^T M \Sigma_P) + \|M\mu_P + c\|^2. \quad (57)$$

In particular, $\|T\|_{L^2(P)}^2$ depends on P only through its first two moments.

Proof. Expanding the squared norm:

$$\begin{aligned} \|T\|_{L^2(P)}^2 &= \int \|Mx + c\|^2 dP(x) \\ &= \int \|M(x - \mu_P) + (M\mu_P + c)\|^2 dP(x) \\ &= \int \|M(x - \mu_P)\|^2 dP(x) + 2 \underbrace{\langle M\mu_P + c, M \int (x - \mu_P) dP(x) \rangle}_{=0} + \|M\mu_P + c\|^2 \\ &= \int (x - \mu_P)^T M^T M (x - \mu_P) dP(x) + \|M\mu_P + c\|^2 \\ &= \text{Tr}(M^T M \Sigma_P) + \|M\mu_P + c\|^2, \end{aligned}$$

where the last step uses $\mathbb{E}_{x \sim P}[(x - \mu_P)(x - \mu_P)^\top] = \Sigma_P$. □

Lemma D.2 (Gradient Norm Equality). *For any $P \in \mathcal{L}(Q_0)$ and its corresponding Gaussian $G_{\mu, \Sigma}$:*

$$\|\nabla_W \mathbb{B}(P|Q)\|_{L^2(P)}^2 = \|\nabla_W \mathbb{B}(G|G)\|_{L^2(G_{\mu, \Sigma})}^2. \quad (58)$$

Proof. First, define $T_{\text{LS}} = \nabla_W \mathbb{B}(P|Q)$ and $T_{\text{Gaussian}} = \nabla_W \mathbb{B}(G_{\mu, \Sigma}|G)$. By construction, both of these mappings are affine, and by Equation 56 $T_{\text{LS}} = T_{\text{Gaussian}}$. From Lemma D.2, since P and $G_{\mu, \Sigma}$ share the first and second order moments by construction, they are equal, which means,

$$\|\nabla_W \mathbb{B}(P|Q)\|_{L^2(P)}^2 = T_{\text{LS}} = T_{\text{Gaussian}} = \|\nabla_W \mathbb{B}(G|G)\|_{L^2(G_{\mu, \Sigma})}^2,$$

which is the desired result. □

We can now state and prove the following result.

Proposition D.2 (PL Inequality Transfer). *Let $\mathcal{L}(Q_0)$ be a location-scatter family and $\mathcal{Q} = \{Q_k\}_{k=1}^K \subset \mathcal{L}(Q_0)$. Let $\mathcal{G} = \{G_{\mu_k, \Sigma_k}\}_{k=1}^K$ be the corresponding Gaussian with matching moments. If the Bures-Wasserstein barycenter functional $\mathbb{B}(\cdot|\mathcal{G})$ satisfies the PL inequality with constant $C_{\text{PL}} > 0$, i.e.,*

$$\|\nabla_W \mathbb{B}(G_{\mu, \Sigma}|G)\|_{L^2(G_{\mu, \Sigma})}^2 \geq C_{\text{PL}} (\mathbb{B}(G_{\mu, \Sigma}|G) - \mathbb{B}(G_{\mu^*, \Sigma^*}|G)), \quad (59)$$

then $\mathbb{B}(\cdot|\mathcal{Q})$ satisfies the PL inequality on $\mathcal{L}(Q_0)$ with the same constant,

$$\|\nabla_W \mathbb{B}(P|Q)\|_{L^2(P_{m, \Sigma})}^2 \geq C_{\text{PL}} (\mathbb{B}(P|Q) - \mathbb{B}(P^*|Q)). \quad (60)$$

Proof. Starting from the PL inequality for Gaussians (Equation 59):

$$\|\nabla_W \mathbb{B}(G_{\mu, \Sigma}|G)\|_{L^2(G_{\mu, \Sigma})}^2 \geq C_{\text{PL}} (\mathbb{B}(G_{\mu, \Sigma}|G) - \mathbb{B}(G_{\mu^*, \Sigma^*}|G)).$$

Applying Lemma D.2 to the left-hand side:

$$\|\nabla_W \mathbb{B}(P|Q)\|_{L^2(P)}^2 \geq C_{\text{PL}} (\mathbb{B}(G_{\mu, \Sigma}|G) - \mathbb{B}(G_{\mu^*, \Sigma^*}|G)).$$

Applying Equation (53) and barycenter correspondence to the right-hand side:

$$\|\nabla_W \mathbb{B}(P|Q)\|_{L^2(P)}^2 \geq C_{\text{PL}} (\mathbb{B}(P|Q) - \mathbb{B}(P^*|Q)). \quad \square$$

Explicit PL Constant. By Chewi et al. [2020, Theorem 19], the PL inequality holds for Gaussians under ζ -regularity: if $\|\Sigma_k\|_{\text{op}} \leq 1$ and $\det \Sigma_k \geq \zeta$ for all k , then $C_{\text{PL}} = \zeta^2/4$. Then, Proposition D.2 extends this PL constant to location-scatter families satisfying the same spectral bounds.

Scope and Limitations. Proposition D.2 applies to location-scatter families, which are generated by affine transformations of a base measure. This includes elliptical distributions (e.g., multivariate t -distributions, uniform distributions on ellipsoids) and, importantly, the Swiss roll measures used in our experiments. This result does not directly apply to arbitrary measures.

E DOMAIN ADAPTATION

E.1 INTRODUCTION

Statistical learning theory Vapnik [1999] deals with the problem of learning a function $h : \mathcal{X} \rightarrow \mathcal{Y}$, such that it minimizes the *risk* of making a mistake, that is,

$$h^* = \arg \inf_{h \in \mathcal{H}} \left\{ \mathcal{R}_Q(h) = \int_{\mathcal{X} \times \mathcal{Y}} \mathcal{L}(y, h(x)) dQ(x, y) \right\}, \quad (61)$$

where $P \in \mathcal{P}(\mathcal{X} \times \mathcal{Y})$ is a probability measure, and \mathcal{H} is a family of functions from \mathcal{X} to \mathcal{Y} . $\mathcal{R}_Q(h)$ denotes the risk of h under Q . Equation 61 interprets the learning problem as a minimization problem.

In practical scenarios, one has a dataset $\{x_i^{(Q)}, y_i^{(P)}\}_{i=1}^n, (x_i^{(P)}, y_i^{(Q)}) \stackrel{i.i.d.}{\sim} P$. As a result, one can estimate the *empirical* risk, and consequently minimize it,

$$\hat{h} = \arg \inf_{h \in \mathcal{H}} \left\{ \hat{\mathcal{R}}_Q(h) = \frac{1}{n} \sum_{i=1}^n \mathcal{L}(y_i^{(Q)}, h(x_i^{(Q)})) \right\}, \quad (62)$$

which is the foundation of the *Empirical Risk Minimization (ERM)* framework. In this sense, a solution \hat{h} to equation 62 is said to *generalize* if it achieves low risk $\mathcal{R}_Q(h)$.

There is a fundamental assumption at play in the theory of generalization under the ERM framework. Indeed, both \mathcal{R}_P and $\hat{\mathcal{R}}_P$ evaluate the risk under a fixed probability measure P . However, machine learning models are oftentimes confronted with data following *different, but related* probability measures Quiñero-Candela et al. [2022], a process known as *distribution shift*.

The main tool for tackling distribution shift is *domain adaptation*. This problem considers now two datasets, namely, a labeled source dataset $\{x_i^{(Q_S)}, y_i^{(Q_S)}\}_{i=1}^{n_S}$, and an *unlabeled* target dataset $\{x_j^{(Q_T)}\}_{j=1}^{n_T}$. The goal is to obtain a function h that achieves low risk under Q , with the available data. A natural extension to this problem is *multi-source* domain adaptation, where *multiple source domains* are available, i.e., $\mathcal{Q} = \{Q_k\}_{k=1}^K$, each with its own associated dataset $\{(x_i^{(Q_k)}, y_i^{(Q_k)})\}_{i=1}^{n_k}$.

E.2 SOURCE-ONLY TRAINING

A straightforward baseline in domain adaptation is the *source-only* training. Let $h = g \circ f$ be the composition of a feature extractor $g : \mathcal{X} \rightarrow \mathcal{U}$ and a feature classifier $f : \mathcal{U} \rightarrow \mathcal{Y}$. We can train h *end-to-end* by minimizing,

$$\mathcal{L}(\theta) = \frac{1}{K} \sum_{k=1}^K \frac{1}{n_k} \sum_{i=1}^{n_k} \mathcal{L}(y_i^{(Q_k)}, f(g(x_i^{(Q_k)}))).$$

This training produces an embedding space \mathcal{U} that is discriminative of the classes in the domain adaptation problem. Following previous work Montesuma and Mboula [2021], Montesuma et al. [2023, 2024a], we perform adaptation in this space.

E.3 WASSERSTEIN BARYCENTER TRANSPORT

The motivation for using Wasserstein barycenters in multi-source domain adaptation comes from a theoretical result of Redko et al. [2019]. Indeed, by [Redko et al., 2019, Theorem 2],

$$\mathcal{R}_{Q_T}(h) \leq \mathcal{R}_{Q_S}(h) + \mathbb{W}_1(\hat{Q}_S, \hat{Q}_T) + \mathcal{O}(n_S^{-1/2} + n_T^{-1/2}) + \mathbb{R}(Q_S, Q_T), \quad (63)$$

where $\mathbb{R}(Q_S, Q_T) = \inf_{h \in \mathcal{H}} \mathcal{R}_{Q_S}(h) + \mathcal{R}_{Q_T}(h)$ is the joint risk. This result establishes that when source and target measures are close, their risks are close as well. Now, assume equation 63 holds for each pair (Q_k, Q_T) , then, summing over k weighted by λ_k ,

$$\mathcal{R}_{Q_T}(h) \leq \sum_{k=1}^K \lambda_k \mathcal{R}_{Q_k}(h) + \sum_{k=1}^K \lambda_k \mathbb{W}_1(\hat{Q}_k, \hat{Q}_T) + \mathcal{O}(n^{-1/2}) + \sum_{k=1}^K \lambda_k \mathbb{R}(Q_k, Q_T),$$

using the triangle inequality on $\mathbb{W}_1(\hat{Q}_k, \hat{Q}_T)$

$$\mathcal{R}_{Q_T}(h) \leq \sum_{k=1}^K \lambda_k \mathcal{R}_{Q_k}(h) + \sum_{k=1}^K \lambda_k \mathbb{W}_1(\hat{Q}_k, P) + \mathbb{W}_1(P, \hat{Q}_T) + \mathcal{O}(n^{-1/2}) + \sum_{k=1}^K \lambda_k \mathbb{R}(Q_k, Q_T),$$

A reasonable choice to make this bound tight is choosing P that minimizes $P \mapsto \sum_{k=1}^K \lambda_k \mathbb{W}_1(\hat{Q}_k, P) + \mathbb{W}_1(P, \hat{Q}_T)$.

From $p = 1$ to $p > 1$. The argument for $p > 1$ is a bit more intricate. Since \mathbb{W}_1 is the weakest of the Wasserstein distances [Villani, 2008, Remark 6.6], we can directly move from $p = 1$ to $p > 1$,

$$\mathcal{R}_{Q_T}(h) \leq \sum_{k=1}^K \lambda_k \mathcal{R}_{Q_k}(h) + \sum_{k=1}^K \lambda_k \mathbb{W}_p(\hat{Q}_k, \hat{Q}_T) + \mathcal{O}(n^{-1/2}) + \sum_{k=1}^K \lambda_k \mathbb{R}(Q_k, Q_T),$$

which, from the triangle inequality, results in,

$$\mathcal{R}_{Q_T}(h) \leq \sum_{k=1}^K \lambda_k \mathcal{R}_{Q_k}(h) + \sum_{k=1}^K \lambda_k \mathbb{W}_p(\hat{Q}_k, P) + \mathbb{W}_p(P, \hat{Q}_T) + \mathcal{O}(n^{-1/2}) + \sum_{k=1}^K \lambda_k \mathbb{R}(Q_k, Q_T), \quad (64)$$

The term $\sum_{k=1}^K \lambda_k \mathbb{W}_p(\hat{Q}_k, P) + \mathbb{W}_p(P, \hat{Q}_T)$ does not correspond to the p -Wasserstein barycenter due the missing power of p . We can retrieve it through Young's inequality for products. Let $a, b > 0$ be real numbers, and $p, q > 1$. Then $ab \leq \frac{a^p}{p} + \frac{b^q}{q}$. We can get the inequality,

$$\mathbb{W}_p(\hat{P}, \hat{Q}) \leq \frac{\mathbb{W}_p(\hat{P}, \hat{Q})^p}{p} + \frac{p-1}{p},$$

by letting $a = \mathbb{W}_p(\hat{P}, \hat{Q})$, $b = 1$ and $q = \frac{p}{p-1}$. We apply this inequality to the $K+1$ terms in the previous bound. More precisely,

$$\mathbb{W}_p(\hat{Q}_k, P) \leq \frac{1}{p} \mathbb{W}_p(\hat{Q}_k, P)^p + \frac{p-1}{p}, \text{ and } \mathbb{W}_p(P, \hat{Q}_T) \leq \frac{1}{p} \mathbb{W}_p(P, \hat{Q}_T)^p + \frac{p-1}{p}$$

Plugging this back into inequality 64,

$$\mathcal{R}_{Q_T}(h) \leq \sum_{k=1}^K \lambda_k \mathcal{R}_{Q_k}(h) + \frac{1}{p} \left(\sum_{k=1}^K \lambda_k \mathbb{W}_p(\hat{Q}_k, P)^p + \mathbb{W}_p(P, \hat{Q}_T)^p \right) + \frac{2(p-1)}{p} + \mathcal{O}(n^{-1/2}) + \sum_{k=1}^K \lambda_k \mathbb{R}(Q_k, Q_T).$$

Modulo some additional constants depending on $p > 1$, we have the same reasoning as $p = 1$.

Wasserstein Barycenter Transport ($p = 2$). Montesuma and Mboula [2021] uses a two-step procedure for finding P . First, one solves,

$$P^* = \arg \min_{P \in \mathcal{P}_{1,ac}(\Omega)} \sum_{k=1}^K \lambda_k \mathbb{W}_2(Q_k, P)^2,$$

which is the 2-Wasserstein barycenter problem. Then, one aligns the barycenter with the target domain through OT. This is done through the barycenter mapping,

$$\gamma^* = \arg \min_{\gamma \in \Gamma(P, \hat{Q}_T)} \sum_{i=1}^n \sum_{j=1}^{n_T} \gamma_{ij} \|x_i^{(P)} - x_j^{(Q_T)}\|_2^2, \quad (65)$$

Algorithm 2 Wasserstein Barycenter Transport

Input: $\mathcal{Q} = \{Q_k\}_{k=1}^K$, $Q_k \in \mathcal{P}_2(\mathcal{X} \times \mathcal{Y})$, $Q_T \in \mathcal{P}_2(\mathcal{X})$, $\lambda \in \Delta_K$

Output: Labeled target domain data $\{T_{P \rightarrow Q_T}(x_i^{(P)}), y_i^{(P)}\}_{i=1}^n$

- 1: **for** $\tau \leftarrow 1$ to n_{iter} **do**
 - 2: Compute $P^* = \text{Bar}(\lambda, \mathcal{Q})$
 - 3: Compute γ^* between P^* and Q_T (eq. 65)
 - 4: Transport $(x_i^{(P)}, y_i^{(P)})$ (eq. 66)
 - 5: **end for**
-

and,

$$T_{P \rightarrow Q_T}(x_i^{(P)}) = n_T \sum_{j=1}^{n_T} \gamma_{ij}^* x_j^{(Q_T)}, \quad (66)$$

which is the minimizer of $P \mapsto \mathbb{W}_2(P, \hat{Q}_T)^2$. We provide an algorithm for this strategy in Algorithm 2. Note that since this procedure generates a labeled dataset on data following the target domain measure, we can train a classifier with the pairs $\{T_{P \rightarrow Q_T}(x_i^{(P)}), y_i^{(P)}\}$.

E.4 ADAPTING NEURAL NETWORK BARYCENTER SOLVERS TO DA

Here, we cover *how* we adapted previous neural network-based barycenters to perform domain adaptation. There is one main challenge with using unlabeled barycenters for domain adaptation: we cannot directly move the barycenter to the target domain, as we would end up with more unlabeled data. A straightforward solution to this problem is moving the available labeled data that we have, that is, the source domain data. For this scenario, the barycenter domain works as a *pivot domain*, as we transport the source to the target through the composition,

$$T_{Q_k \rightarrow Q_T}(x_i^{(Q_k)}) = T_{P \rightarrow Q_T}(T_{Q_k \rightarrow P}(x_i^{(Q_k)})). \quad (67)$$

In comparison, by computing a *labeled barycenter*, we synthesize data in P^* .

As we demonstrated in Tables 3 through 7, this is generally beneficial for domain adaptation. In this way, we can acquire a labeled dataset in the target domain through $\{\{T_{P \rightarrow Q_T}(T_{Q_k \rightarrow P}(x_i^{(Q_k)})), y_i^{(Q_k)}\}_{i=1}^{n_k}\}_{k=1}^K$. To isolate the effect of the quality of the computed barycenters, we estimate the mappings as we did in equations 65 and 66, that is,

$$T_{Q_k \rightarrow P}(x_i^{(Q_k)}) = n \sum_{j=1}^n \gamma_{k,i,j}^* x_j^{(P)} \quad T_{P \rightarrow Q_k}(x_i^{(P)}) = n_T \sum_{j=1}^{n_T} \gamma_{ij}^* x_j^{(Q_T)}, \quad (68)$$

where γ_k^* is the OT plan from Q_k to P , and γ^* is the OT plan from P to Q_T .

F ADDITIONAL EXPERIMENTS

In total, we compare five domain adaptation benchmarks, divided into computer vision, neuroscience and chemical engineering. An overview of the benchmarks is presented in Table 1 in our main paper. Here, we give further details on each of the benchmarks. For **computer vision**, we use the Office 31 Saenko et al. [2010] and Office Home Venkateswara et al. [2017] benchmarks. For neuroscience, we use the BCI-CIV-2a Brunner et al. [2008] and ISRUC Khalighi et al. [2013] benchmarks. For chemical engineering, we use the TEP benchmark Montesuma et al. [2024c].

F.1 EVALUATION PROTOCOL AND BACKBONES

As we describe in the following, all benchmarks deal with multi-class classification. We measure performance using the standard classification accuracy,

$$\text{accuracy}(y, \hat{y}) = \frac{1}{n} \sum_{i=1}^n \delta(y_i - \hat{y}_i) \times 100\%.$$

For the Office 31, Office Home, Tennessee Eastman Process, and BCI-CIV-2a, we adopt the so-called *leave-one-domain-out* evaluation. For example, given 3 domains $\{A, B, C\}$, we perform 3 experiments, leaving one domain as the target domain at each time. Then, one of these experiments would be $\{A, B\} \rightarrow C$, where $\{A, B\}$ are the sources, and C is the target.

As we discuss in the main paper, we perform adaptation over embeddings. To that end, we use the same experimental setting as Montesuma et al. [2024b] for the Office 31, Office Home, and TEP benchmarks. More specifically, we train a ResNet 50 and ResNet 101 for the Office 31 and Office Home benchmarks, and a CNN for the TEP benchmark. For this latter backbone, we refer readers to Montesuma et al. [2024c] for further details. For neuroscience benchmarks, we follow the experimental protocol of Wang et al. [2024], where we fine-tune CBraMod, a transformer-based foundation model, on available source domain data. We use the exact same training settings as these authors.

F.2 FINE-GRAINED RESULTS

Office 31 Saenko et al. [2010] contains, in total, 4652 images among 31 classes of objects. These images are divided into 3 different domains: *Amazon*, *dSLR*, and *Webcam*. Images in the *Amazon* domain represent products, usually with an homogeneous background, medium resolution, and studio lightning. There are 2817 images in this domain. The *dSLR* domain contains high-resolution images obtained through a digital SLR camera in an office environment. There are 498 images in this domain. Finally, the *Webcam* domain contains images of objects captured with a webcam, also in an office environment. There 795 images in this domain. As analyzed in Ringwald and Stiefel-hagen [2021], this benchmark is one of the most commonly used in the literature. Despite its moderate size, it presents challenges of its own. For instance, since the *Amazon* domain images were collected automatically, it has label noise.

We show our results in the Office 31 benchmark in Table 3. Overall, dictionary learning methods such as DaDiL Montesuma et al. [2023] or GMM-DaDiL Montesuma et al. [2024b] remain state-of-the-art for this benchmark. However, our gradient flow algorithm is able to improve previous methods, closing the gap between these two kinds of algorithms. In comparison with *unsupervised barycenters*, using labels in the ground-cost ($\mathcal{X} \times \mathcal{Y} = \checkmark$) has a clear advantage.

Office-Home Venkateswara et al. [2017] contains, 15,500 images among 65 classes of objects. There are four domains: *Art*, *Clipart*, *Product*, and *Real-World*. The *Art* domain contains artistic depictions of objects, such as sketches, paintings, and ornamentation. It has 2427 images. The *Clipart* domain is a collection of graphic art representing the objects. This domain has 4365 images. *Product* contains images of objects without a background. It has 4439 images. *Real-World* contains images of objects captured with a camera. It contains 4357 images. In this sense, the *Product* domain is similar to the *Amazon* domain in the Office 31 benchmark, and the *Real-World* is similar to *dSLR* or *Webcam*. In comparison with the *Office31* benchmark, the *Office-Home* benchmark adds another factor of domain variation: style (e.g., *Art* vs. *Real-World*). We show our results in Table 4. In comparison with the *Office 31* benchmark, our methods get even closer to the state-of-the-art. Again, using labels in the ground cost ($\mathcal{X} \times \mathcal{Y} = \checkmark$) offers a clear advantage.

Remark F.1. We follow previous works on visual domain adaptation, especially Saenko et al. [2010] and Venkateswara et al. [2017], and report the classification accuracy on fixed partitions of the target domains. For that reason, Tables 3 and 4 do not have confidence intervals. While it would be possible to run these experiments with random partitions (e.g., k -fold cross validation), this would mean that our results would not be comparable to previous established results in Montesuma et al. [2024b], for instance.

Tennessee-Eastman Process (TEP) [Reinartz et al., 2021, Montesuma et al., 2024c] is a benchmark in chemical engineering. This benchmark comprises a set of simulations of a chemical reaction that occurs inside a reactor. In total, 34 variables are measured over time. As a result, we have a set of time-series representing how the reaction progresses over each simulation. In some of these simulations, one of 28 possible faults can be introduced. The goal is, based on the readings, to determine *which kind of fault*, or its absence, has occurred. As a result, there are 29 classes. Each simulation is also associated with a production mode, which drastically changes the statistical properties of the data generation process, thus introducing a distribution shift. As a result, each domain corresponds to one of these modes of operation. We refer readers to Montesuma et al. [2024c] and Reinartz et al. [2021] for more details.

We report our results in Table 5. For this benchmark, the gap between unlabeled ($\mathcal{X} \times \mathcal{Y} = \mathbf{X}$) and labeled ($\mathcal{X} \times \mathcal{Y} = \checkmark$) barycenter methods is closer. For instance, CW2B Korotin et al. [2021] achieves 85.83 for the average target domain

Algorithm	$\mathcal{X} \times \mathcal{Y}$	A	D	W	Avg. \uparrow
ResNet50	-	67.50	95.00	96.83	86.40
WJDOT Turrisi et al. [2022]	-	67.77	97.32	95.32	86.80
DaDiL-E Montesuma et al. [2023]	-	70.55	100.00	98.83	89.79
DaDiL-R Montesuma et al. [2023]	-	70.90	100.00	98.83	89.91
GMM-DaDiL Montesuma et al. [2024b]	-	72.47	100.00	99.41	90.63
Discrete Cuturi and Doucet [2014]	\mathbf{X}	70.55	96.43	96.49	87.82
NormFlow Visentin and Cheridito [2025]	\mathbf{X}	65.67	97.32	94.73	85.91
CW2B Korotin et al. [2021]	\mathbf{X}	69.16	94.64	95.32	86.37
NOT Kolesov et al. [2024]	\mathbf{X}	69.33	92.85	96.49	86.22
U-NOT Gazdieva et al. [2024]	\mathbf{X}	68.29	97.32	95.32	86.97
WGF (ours)	\mathbf{X}	69.16	98.21	96.49	87.96
Discrete Montesuma et al. [2023]	\checkmark	67.94	98.21	97.66	87.93
GMM Montesuma et al. [2024b]	\checkmark	70.13	99.11	96.49	88.54
WGF (ours)	\checkmark	70.03	99.11	99.41	89.52

Table 3: Classification accuracy per domain for the Office 31 benchmark.

Algorithm	$\mathcal{X} \times \mathcal{Y}$	Ar	Cl	Pr	Rw	Avg. \uparrow
ResNet101	-	72.90	62.20	83.70	85.00	75.95
WJDOT Turrisi et al. [2022]	-	74.28	63.80	83.78	84.52	76.59
DaDiL-E Montesuma et al. [2023]	-	77.16	64.95	85.47	84.97	78.14
DaDiL-R Montesuma et al. [2023]	-	75.92	64.83	85.36	85.32	77.86
GMM-DaDiL Montesuma et al. [2024b]	-	77.16	66.21	86.15	85.32	78.81
Discrete Cuturi and Doucet [2014]	\mathbf{X}	76.13	63.91	83.11	85.55	77.17
NormFlow Visentin and Cheridito [2025]	\mathbf{X}	77.16	62.54	83.10	84.63	76.86
CW2B Korotin et al. [2021]	\mathbf{X}	74.69	63.46	82.54	85.09	76.44
NOT Kolesov et al. [2024]	\mathbf{X}	72.22	63.57	82.77	82.91	75.36
U-NOT Gazdieva et al. [2024]	\mathbf{X}	75.30	64.94	82.88	84.28	76.85
WGF (ours)	\mathbf{X}	74.89	64.60	83.89	85.21	77.56
Discrete Montesuma et al. [2023]	\checkmark	76.54	63.91	83.78	84.74	77.25
GMM Montesuma et al. [2024b]	\checkmark	75.31	64.26	86.71	85.21	77.87
WGF (ours)	\checkmark	76.13	65.52	85.81	86.24	78.42

Table 4: Classification accuracy per domain for the Office-Home benchmark.

Algorithm	$\mathcal{X} \times \mathcal{Y}$	Mode 1	Mode 2	Mode 3	Mode 4	Mode 5	Mode 6	Avg. \uparrow
CNN [†]	-	80.82 \pm 0.96	63.69 \pm 1.71	87.47 \pm 0.99	79.96 \pm 1.07	74.44 \pm 1.52	84.53 \pm 1.12	78.48
WJDOT Turrisi et al. [2022]	-	89.06 \pm 1.34	75.60 \pm 1.84	89.99 \pm 0.86	89.38 \pm 0.77	85.32 \pm 1.29	87.43 \pm 1.23	86.13
DaDiL-E [‡] Montesuma et al. [2023]	-	90.45 \pm 1.02	77.08 \pm 1.21	86.79 \pm 2.14	89.01 \pm 1.35	84.04 \pm 3.16	87.85 \pm 1.06	85.87
DaDiL-R [‡] Montesuma et al. [2023]	-	91.97 \pm 1.22	77.15 \pm 1.32	85.41 \pm 1.69	89.39 \pm 1.03	84.49 \pm 1.95	88.44 \pm 1.29	86.14
GMM-DaDiL Montesuma et al. [2024b]	-	91.72 \pm 1.41	76.41 \pm 1.89	89.68 \pm 1.49	89.18 \pm 1.17	86.05 \pm 1.46	88.02 \pm 1.12	86.85
Discrete Cuturi and Doucet [2014]	\times	90.38 \pm 1.29	71.17 \pm 1.26	85.27 \pm 1.09	87.29 \pm 0.99	83.83 \pm 1.74	84.94 \pm 1.87	83.81
NormFlow Visentin and Cheridito [2025]	\times	87.06 \pm 0.57	66.25 \pm 1.11	88.58 \pm 1.00	89.35 \pm 0.34	80.99 \pm 2.21	85.08 \pm 1.45	82.89
CW2B Korotin et al. [2021]	\times	91.72 \pm 0.79	73.71 \pm 1.42	88.37 \pm 1.31	89.32 \pm 1.14	84.66 \pm 1.75	87.19 \pm 1.24	85.83
NOT Kolesov et al. [2024]	\times	90.31 \pm 1.08	72.37 \pm 0.94	87.99 \pm 1.31	89.28 \pm 0.81	84.35 \pm 1.68	85.29 \pm 2.02	84.93
U-NOT Gazdieva et al. [2024]	\times	90.82 \pm 0.65	72.68 \pm 1.58	88.65 \pm 0.95	89.00 \pm 1.28	85.22 \pm 1.07	86.19 \pm 1.70	85.43
WGF (ours)	\times	91.51 \pm 1.32	73.77 \pm 1.24	87.44 \pm 1.16	89.38 \pm 0.62	84.87 \pm 1.75	86.08 \pm 2.23	85.51
Discrete Montesuma et al. [2023]	\checkmark	92.38 \pm 0.66	73.74 \pm 1.07	88.89 \pm 0.85	89.38 \pm 1.26	85.53 \pm 1.35	86.60 \pm 1.63	86.09
GMM Montesuma et al. [2024b]	\checkmark	92.23 \pm 0.70	71.81 \pm 1.78	84.72 \pm 1.92	89.28 \pm 1.55	87.51 \pm 1.73	82.49 \pm 1.81	84.67
WGF (ours)	\checkmark	92.34 \pm 1.05	76.10 \pm 1.56	89.78 \pm 0.90	89.32 \pm 1.03	85.92 \pm 1.35	87.74 \pm 1.52	86.87

Table 5: Classification accuracy per domain on the Tennessee Eastman Process benchmark.

performance versus 86.09 for the labeled discrete barycenter. Furthermore, it surpasses the GMM method of Montesuma et al. [2024b]. In comparison, our methods establish a new state-of-the-art for barycenter-based domain adaptation in this benchmark, having similar performance to GMM-DaDiL Montesuma et al. [2024b].

BCI-CIV-2a Brunner et al. [2008] Contains electroencephalogram (EEG) data from nine subjects. In brief, an EEG measures the electrical activity of the brain over time. As such, like the TEP benchmark, this benchmark has a collection of time series data. The BCI-CIV-2a data is concerned with motor imagery tasks, that is, the imagination of movement of the left hand, right hand, both feet, and tongue. These correspond to class 1, 2, 3, and 4. Therefore, in this benchmark we have four classes. Our goal here is to perform *cross-subject* adaptation, namely, we use data from a given set of source subjects, and try to predict on a target subject. Therefore, each domain is a subject, so there are nine domains in total. There are, on average, 560 samples per subject, with a total of 5088 samples.

Algorithm	$\mathcal{X} \times \mathcal{Y}$	1	2	3	4	5	6	7	8	9	Avg. \uparrow
CBraMod [†]	-	52.22	40.45	64.23	40.41	47.74	48.34	53.64	50.52	55.03	50.30
DaDiL-R [‡] Montesuma et al. [2023]	-	58.68	40.27	66.14	41.45	59.54	51.38	53.12	57.46	55.21	53.69
GMM-DaDiL Montesuma et al. [2024b]	-	60.59	42.36	70.31	48.12	61.11	50.34	62.15	58.85	60.00	57.10
Discrete Cuturi and Doucet [2014]	\times	60.93	43.40	69.96	50.00	61.28	50.69	61.63	61.45	57.11	57.38
NormFlow Visentin and Cheridito [2025]	\times	57.11	43.22	67.53	47.71	60.24	51.04	56.25	60.76	55.20	55.45
CW2B Korotin et al. [2021]	\times	60.00	43.57	70.13	48.95	60.93	51.21	61.28	61.63	57.46	57.25
NOT Kolesov et al. [2024]	\times	61.28	43.22	70.31	47.91	60.59	51.21	61.46	61.80	57.29	57.23
U-NOT Gazdieva et al. [2024]	\times	60.59	44.09	69.44	47.70	61.11	50.34	61.97	61.11	58.15	57.17
WGF (ours)	\times	60.93	43.75	69.96	49.16	60.76	51.38	61.97	63.54	57.64	57.68
Discrete Montesuma et al. [2023]	\checkmark	60.76	42.53	70.66	48.54	61.28	50.69	61.63	61.28	59.54	57.43
GMM Montesuma et al. [2024b]	\checkmark	60.59	42.53	69.79	47.08	61.45	50.34	62.32	59.54	59.72	57.04
WGF (ours)	\checkmark	60.93	46.18	68.92	50.21	62.32	50.69	61.63	61.11	57.11	57.68

Table 6: Classification accuracy per domain on the BCI-CIV-2a benchmark.

We show our results in Table 6. For cross-subject studies, we highlight that, besides improving individual domain performance, it is desirable to not degrade over the source-only performance. This is indeed the case for almost all methods. For instance, DaDiL Montesuma et al. [2023] degrades performance of subjects 2 and 7 by a small margin. For this benchmark, the difference between unlabeled ($\mathcal{X} \times \mathcal{Y} = \times$) and labeled ($\mathcal{X} \times \mathcal{Y} = \checkmark$) is not as marked as before. We hypothesize that this benchmark falls into the covariate shift hypothesis, namely, $Q_S(X) \neq Q_T(X)$, rather than the more general joint shift $Q_S(X, Y) \neq Q_T(X, Y)$.

ISRUC Khalighi et al. [2013] is a benchmark for EEG data for sleep staging. In brief, sleep staging is the classification of physiological data, such as EEG, recorded during sleep into different sleep stages. In this context, the ISRUC benchmark is the most large scale benchmark used in this paper. This study comprises 100 subjects, with a total of 89240 samples (approximately 900 samples per domain). The sleep staging problem in this benchmark has five classes: awake, non-rapid eye movement sleep (subdivided into N1, N2, N3), and rapid eye movement sleep.

Algorithm	$\mathcal{X} \times \mathcal{Y}$	1	2	3	4	5	6	7	8	9	10	Avg. \uparrow
CBraMod [†]	-	78.97	80.35	70.46	85.59	80.69	72.85	77.00	73.29	83.41	68.95	76.63
WJDOT Turrisi et al. [2022]	-	80.41	78.25	65.69	82.85	81.74	77.74	76.33	68.75	86.95	70.81	76.95
DaDiL-E Montesuma et al. [2023]	-	76.12	77.90	65.93	83.21	81.28	68.45	75.66	72.61	79.75	65.93	75.14
DaDiL-R Montesuma et al. [2023]	-	78.06	78.13	66.97	84.64	81.51	72.02	76.33	72.84	80.85	67.55	75.89
GMM-DaDiL Montesuma et al. [2024b]	-	76.63	78.95	66.51	82.73	77.44	73.81	77.00	71.70	83.05	66.86	75.47
Discrete Cuturi and Doucet [2014]	\times	78.77	80.58	69.76	85.83	79.06	73.45	78.33	72.50	84.14	68.48	77.09
NormFlow Visentin and Cheridito [2025]	\times	81.12	82.90	75.58	84.28	80.34	78.69	75.88	70.34	80.48	70.81	78.05
CW2B Korotin et al. [2021]	\times	79.08	78.25	69.07	86.54	78.48	70.35	76.88	70.90	82.80	66.04	75.84
NOT Kolesov et al. [2024]	\times	78.57	79.88	67.32	85.59	78.72	73.21	77.77	72.50	83.41	67.21	76.44
U-NOT Gazdieva et al. [2024]	\times	80.20	83.48	73.72	87.50	76.51	72.62	76.66	70.22	78.17	71.51	77.06
WGF (ours)	\times	79.69	81.86	70.58	86.66	78.14	77.74	78.77	72.16	85.97	70.00	78.16
Discrete Montesuma et al. [2023]	\checkmark	78.87	80.69	72.09	86.07	78.60	78.45	78.00	72.95	85.48	70.81	78.20
GMM Montesuma et al. [2024b]	\checkmark	75.20	75.46	69.88	80.71	78.60	71.90	76.33	68.41	78.17	68.14	74.28
WGF (ours)	\checkmark	80.10	80.81	76.62	85.95	76.86	80.35	76.55	77.72	84.87	73.95	80.02

Table 7: Classification accuracy per domain on the ISRUC benchmark.

Due the elevated number of subjects in this benchmark, we adopt a slightly different evaluation protocol. Instead of using the *leave-of-domain-out* strategy, we fix the first 90 subjects as *training subjects* and evaluate the performance of adapting to the remaining 10 subjects. This means that we compute Wasserstein barycenters of $K = 90$ input measures. Overall, our WGF method has clear advantage over all other methods, with unsupervised WGF (78.16% average target accuracy) being the best over unlabeled barycenters, and labeled barycenters as well (80.02% average test accuracy).

E.3 COMPLEXITY ANALYSIS AND ADDITIONAL RUNNING TIME

We start with analyzing the complexity of *evaluating* the functionals used in our work. We recall that,

$$\mathbb{V}(P) = \frac{1}{n} \sum_{i=1}^n V(z_i^{(P)}), \quad \mathbb{U}(P) = \frac{1}{n^2} \sum_{i=1}^n \sum_{j=1}^n U(z_i^{(P)}, z_j^{(P)}),$$

where, assuming that the complexity of evaluating V and U is $\mathcal{O}(1)$, the complexity of evaluating \mathbb{V} is $\mathcal{O}(n)$ and for \mathbb{U} is $\mathcal{O}(n^2)$. The complexity of \mathbb{B} is usually the bottleneck, as it involves computing K OT problems. For exact OT, this means we need to solve K OT problems of size $m \times n$, where m is the batch size and n is the barycenter support size. These OT problems need to be solved sequentially, as parallelizing K independent linear programs is non-trivial. In practice, we use the network simplex solver of Bonneel et al. [2011], wrapped in Python by Flamary et al. [2021]. This algorithm has worst-case complexity of $\mathcal{O}(n^3)$ but in practice, runs in $\mathcal{O}(n^2)$. Assuming $n \gg m$, the complexity becomes,

$$\text{Exact barycenter functional complexity} = \mathcal{O}(K \times m \times n),$$

which scales linearly with the barycenter support size n . Though this might appear contradictory with the usual $\mathcal{O}(n^3)$ complexity of OT, we highlight that we are keeping m constant as we scale the barycenter support size n . The same analysis can be done for entropic OT,

$$\text{Entropic barycenter functional complexity} = \mathcal{O}(K \times L \times m \times n),$$

where, instead of a factor m^2 , we have $L \times m$, where $L > 0$ is the number of Sinkhorn iterations. Both of these approaches scale linearly with the number of samples in the barycenter support. However, there are 2 important advantages of using entropic OT. First, we can use GPU acceleration for computing the OT variables. Second, as we shown in Section 3.1, we can vectorize the K OT problems. While this does not alleviate the K term in the complexity, it does lead to further speedups. These factors explain the difference, in running time, between exact and entropic OT.

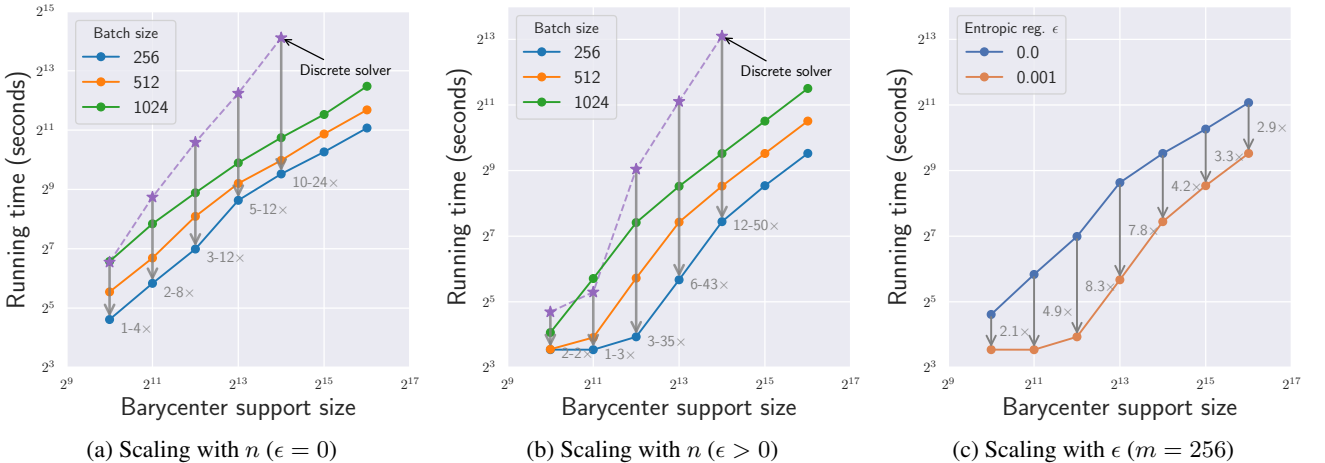


Figure 8: Running time analysis in the Swiss roll example. In (a) and (b), we show that our WGF approach improves the scaling of the discrete solver of Cuturi and Doucet [2014]. In (c), we isolate the speedups of GPU parallelism and Sinkhorn vectorization.

Next, we perform a running time analysis of the tested methods on the ISRUC benchmark, which contains the most number of samples and domains. For all neural net methods, we fix a batch size of 256 samples. Overall, our proposed methods run significantly faster than previous methods. For instance, in comparison with the discrete solver of Cuturi and Doucet [2014],

our algorithm is approximately seven times faster *per iteration*. It is noteworthy that some neural net methods are relatively faster per iteration (e.g. NormFlow). However, we empirically verified that these methods sometimes need a large number of iterations to converge to a good barycenter (e.g. 5000 iterations).

Method	Complexity per iteration	Parameter Complexity	Running time per iteration (s)	# Iterations	Running Time (s)
Discrete Cuturi and Doucet [2014], Montesuma et al. [2023]	$Kn^3 \log n$	n	4.28	50	214.37
NormFlow Visentin and Cheridito [2025]	N/A	$ f $	0.17	5000	878.32
CW2B Korotin et al. [2021]	N/A	$K(f + g)$	2.18	1000	2181.00
NOT Kolesov et al. [2024]	N/A	$K(f + g)$	41.63	25	1040.75
U-NOT Gazdieva et al. [2024]	N/A	$K(f + g)$	13.29	100	1329.77
WGF (ours, $\epsilon = 0$)	Km^2n	n	0.05	200	10.43
WGF (ours, $\epsilon = 10^{-3}$)	$KLmn$	n	0.03	200	7.00

Table 8: Complexity and running time (in seconds) of different barycenter calculation strategies on the ISRUC benchmark. n_b denotes the batch size, n number of samples, K number of input measures, d number of dimensions. For NormFlow, f denotes the neural net implementing the normalizing flow. For CW2B, NOT and U-NOT, f and g denote the neural networks approximating the Kantorovich potentials. $|f|$ and $|g|$ denote the number of their parameters.

F.4 EFFECT OF DIFFERENT FUNCTIONALS

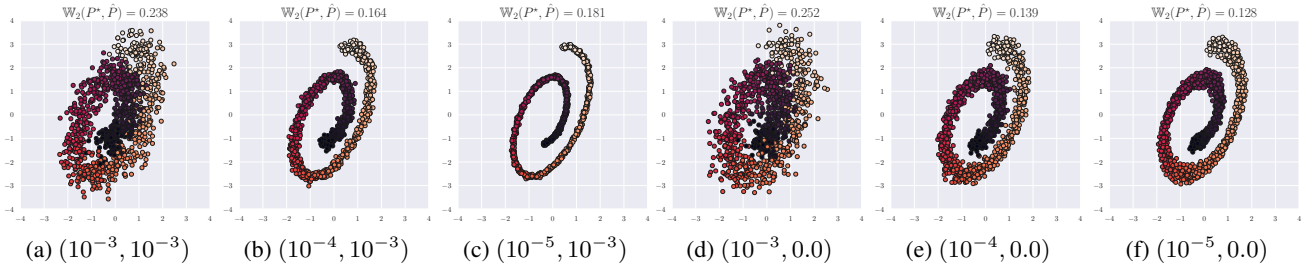


Figure 9: Wasserstein barycenter as a function of (η_G, ϵ) , i.e., diffusion coefficient ξ , and entropy regularization ϵ .

On the effect of \mathbb{G} . The internal energy functional [Chizat, 2025] controls the smoothness of \mathbb{G} , and acts, in the case of the entropy functional $G(s) = s \log s$, as a diffusion term. In Figure 9, we show the effect of varying ξ (c.f. equation 16) in the final barycenter. Overall, an aggressive diffusion coefficient leads to fuzzy barycenters (c.f. Figure 9 (a)), while a coefficient too small leads to low variance measures (c.f. Figure 9 (c)). This is, in fact, an artifact of the entropic OT. While a large diffusion coefficient does lead to fuzzy barycenters with exact OT (c.f. Figure 9 (d)), using a small coefficient does not degrade the quality of the computed barycenter.

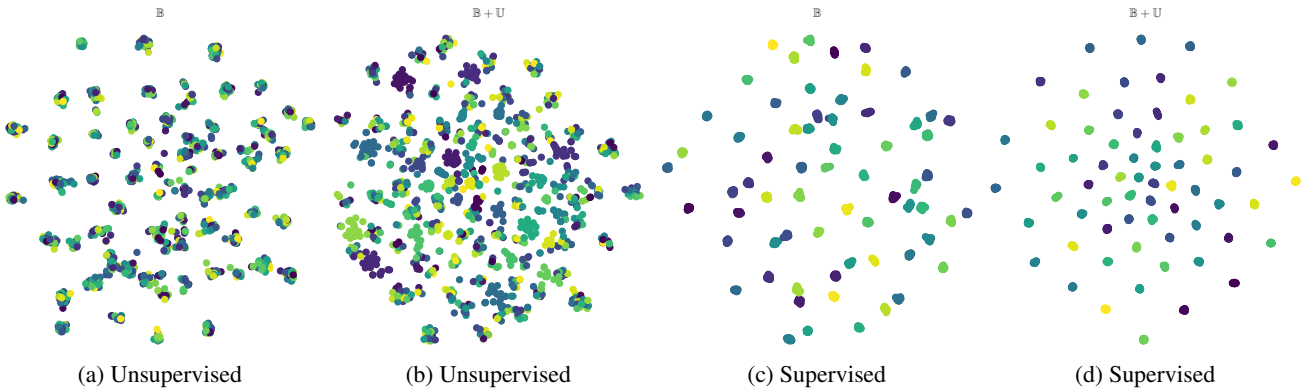


Figure 10: t-SNE embeddings of unsupervised (a, b) and supervised (c, d) barycenters. While it is possible to group some samples according to their pseudo-labels based on \mathbb{U} , the task is in general difficult. For the supervised case, the interaction energy is able to make classes more separable (d, in comparison to c).

On the effect of \mathbb{U} . We now visualize the effect of adding the repulsion interaction energy functional in the Office-Home benchmark. For computer vision experiments we use ResNets [He et al., 2016] as the backbone, which produce

2048-dimensional embeddings. For that reason, we use the cosine distance $d(x, x') = 1 - \text{cossim}(x, x')$ in equation 22 and we fix $\text{margin} = 1$, which encourages class clusters to live in orthogonal sub-spaces of the latent space. Overall, adding \mathbb{U} leads to well separated classes.

In Figure 10, we show a comparison between unsupervised and supervised regularized barycenters. In (a), unsupervised, unregularized barycenters do not have any label structure, since there is no label supervision. In (b), we show that by adding the interaction energy functional, we can cluster samples with the same assigned label – even without input measure label supervision. In (c) and (d), we show the supervised case, in which labels in the input measures are available. In (c), classes are well clustered, but some of them overlap in the embedding space. Adding the interaction energy functional \mathbb{U} effectively pushes these apart, as shown in (d). Overall, we conclude that *enforcing well separated class clusters is not straightforward without the inductive bias coming from the labels*.

On the effect of \mathbb{V} . In Figure 11, we show the distribution of label entropy values (c.f. equation 22) as a function of the potential scaling η ,

$$\mathbb{V}(P) = \frac{\eta}{n} \sum_{i=1}^n V(y_i^{(P)}).$$

We see that increasing the weight of this functional leads to increasingly sharp labels.

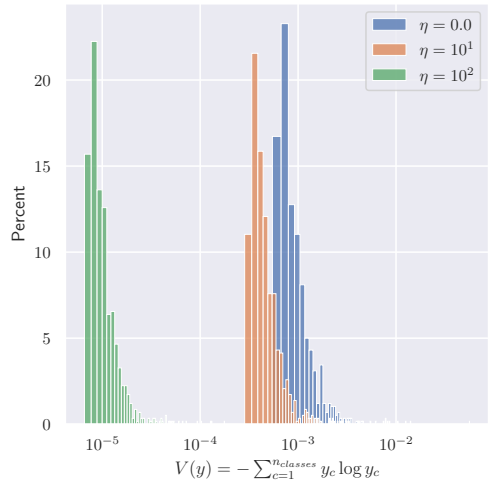


Figure 11: Distribution of label entropy values as a function of potential energy scaling η .

F.5 HYPERPARAMETER SETTING

In this section, we detail the hyperparameters of our methods. For both flows, we have mainly three parameters,

- number of samples in the barycenter support, n .
- learning rate α for the gradient flow,
- number of iterations n_{iter} ,

additionally, for the empirical flow, we have the batch size m for the input measures. We show the complete list of hyperparameters in Table 9. Additionally to these parameters, we also have the choice of regularizing functionals, \mathbb{V} and \mathbb{U} .

Benchmark	n	m	α	n_{iter}	ϵ	\mathbb{V}	η_V	\mathbb{U}	η_U	margin	η_G
Supervised ($\mathcal{X} \times \mathcal{Y}$)											
Office31	620	620	1.0	100	10^{-3}	Entropy	10^2	Repulsion	10^3	1.0	10^{-2}
Office-Home	1300	325	1.0	100	10^{-3}	-	-	Repulsion	10^5	1.0	10^{-4}
TEP	870	145	1.0	50	0.0	Entropy	10^2	Repulsion	10^3	1.0	0.0
BCI-CIV-2a	40	80	1.0	50	10^{-2}	Entropy	10^2	Repulsion	10^5	1.0	0.0
ISRUC	200	100	0.1	200	0.0	-	-	-	-	-	-
Unsupervised (\mathcal{X})											
Office31	620	465	1.0	100	10^{-2}	-	-	Repulsion	10^5	1.0	10^{-3}
Office-Home	1950	650	1.0	100	0.0	-	-	Repulsion	10^6	1.0	10^{-2}
TEP	580	145	1.0	50	0.0	-	-	-	-	-	-
BCI-CIV-2a	80	40	1.0	50	10^{-2}	-	-	-	-	-	-
ISRUC	250	50	0.1	200	10^{-3}	-	-	-	-	-	-

Table 9: Hyperparameters used in each benchmark. n denotes number of samples, m denotes the batch size, α denotes learning rate, n_{iter} denotes number of iterations.

We offer some additional reasoning on how to choose these parameters. The number of samples controls the complexity of the calculated barycenter. We express these values in terms of the number of classes. For instance, $n = 1550$ in the Office 31

benchmark translates to $n = 31 \times 50$ samples, that is, 50 samples per class. The same reasoning applies to the batch size m . Furthermore, our method is fairly robust to the choice of learning rate. For instance, as we discussed in section C.1, the fixed-point iterations in the discrete barycenter are equivalent to setting $\alpha = n/2$, where n is the number of samples in the Wasserstein barycenter. This generally strikes a balance on how fast the algorithm converges.

E.6 ABLATION

Table 10 ablates the effect of the functionals \mathbb{G} , \mathbb{V} , \mathbb{U} in the Office-Home benchmark. First, our WGF consistently outperforms the discrete baseline (77.17 vs. 77.53 and 77.24 vs. 78.42 in the unlabeled and labeled cases). Second, \mathbb{V} acts as a stabilizer with high entropic regularization ($\epsilon = 10^{-2}$). While the entropic regularizer blurs the barycentric measure, \mathbb{V} has a sharpness effect. Third, our WGF is more sensitive to the entropic regularization, ϵ , particularly when used as a loss function (our case) rather than for OT plan calculations, as in Cuturi and Doucet [2014]. This latter point highlights the importance of using a sharpness functional. We explore the effects of \mathbb{G} , \mathbb{V} , and \mathbb{U} in further detail in Appendix F.4.

Method	ϵ	\mathbb{B}	$\mathbb{B}+\mathbb{U}$	$\mathbb{B}+\mathbb{V}$	$\mathbb{B}+\mathbb{V}+\mathbb{U}$	$\mathbb{B}+\mathbb{G}$	$\mathbb{B}+\mathbb{G}+\mathbb{V}$	$\mathbb{B}+\mathbb{G}+\mathbb{U}$	$\mathbb{B}+\mathbb{G}+\mathbb{V}+\mathbb{U}$
<i>Unlabeled setting (\mathcal{X} only)</i>									
Discrete	0.0	77.17	—	—	—	—	—	—	—
Discrete	0.01	76.61	—	—	—	—	—	—	—
Discrete	0.001	76.56	—	—	—	—	—	—	—
WGF (ours)	0.0	77.41	76.83	77.41	77.13	76.88	76.88	77.53	77.53
WGF (ours)	0.01	75.54	74.42	75.26	75.26	74.55	74.55	75.00	75.00
WGF (ours)	0.001	77.15	76.88	76.94	76.94	77.28	77.28	77.26	77.26
<i>Labeled setting ($\mathcal{X} \times \mathcal{Y}$)</i>									
Discrete	0.0	77.24	—	—	—	—	—	—	—
Discrete	0.01	76.73	—	—	—	—	—	—	—
Discrete	0.001	76.64	—	—	—	—	—	—	—
WGF (ours)	0.0	77.97	78.12	78.07	78.25	78.11	78.11	78.19	78.19
WGF (ours)	0.01	77.59	77.87	77.83	77.83	77.83	77.88	77.89	77.94
WGF (ours)	0.001	78.16	78.16	78.15	78.16	77.99	78.07	78.42	78.37

Table 10: Ablation on the contribution of each energy functional on domain adaptation performance.